



Theses and Dissertations

2004-08-17

Frequency Estimation of Linear FM Scatterometer Pulses Received by the SeaWinds Calibration Ground Station

Spencer S. Haycock
Brigham Young University - Provo

Follow this and additional works at: <https://scholarsarchive.byu.edu/etd>



Part of the [Electrical and Computer Engineering Commons](#)

BYU ScholarsArchive Citation

Haycock, Spencer S., "Frequency Estimation of Linear FM Scatterometer Pulses Received by the SeaWinds Calibration Ground Station" (2004). *Theses and Dissertations*. 182.
<https://scholarsarchive.byu.edu/etd/182>

This Thesis is brought to you for free and open access by BYU ScholarsArchive. It has been accepted for inclusion in Theses and Dissertations by an authorized administrator of BYU ScholarsArchive. For more information, please contact scholarsarchive@byu.edu, ellen_amatangelo@byu.edu.

FREQUENCY ESTIMATION OF LINEAR FM SCATTEROMETER PULSES
RECEIVED BY THE SEAWINDS CALIBRATION GROUND STATION

by

Spencer S. Haycock

A thesis submitted to the faculty of

Brigham Young University

in partial fulfillment of the requirements for the degree of

Master of Science

Department of Electrical and Computer Engineering

Brigham Young University

December 2004

Copyright © 2004 Spencer S. Haycock

All Rights Reserved

BRIGHAM YOUNG UNIVERSITY

GRADUATE COMMITTEE APPROVAL

of a thesis submitted by

Spencer S. Haycock

This thesis has been read by each member of the following graduate committee and by majority vote has been found to be satisfactory.

8/11/2004
Date

David G. Long
David G. Long, Chair

8/11/2004
Date

Brian D. Jeffs
Brian D. Jeffs

8/11/04
Date

A. Lee Swindlehurst
A. Lee Swindlehurst

BRIGHAM YOUNG UNIVERSITY

As chair of the candidate's graduate committee, I have read the thesis of Spencer S. Haycock in its final form and have found that (1) its format, citations, and bibliographical style are consistent and acceptable and fulfill university and department style requirements; (2) its illustrative materials including figures, tables, and charts are in place; and (3) the final manuscript is satisfactory to the graduate committee and is ready for submission to the university library.

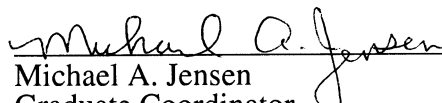
8/11/2004

Date



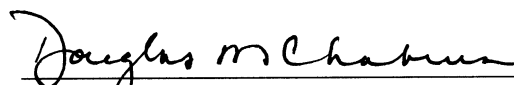
David G. Long
Chair, Graduate Committee

Accepted for the Department



Michael A. Jensen
Graduate Coordinator

Accepted for the College



Douglas M. Chabries
Dean, College of Engineering and Technology

ABSTRACT

FREQUENCY ESTIMATION OF LINEAR FM SCATTEROMETER PULSES RECEIVED BY THE SEAWINDS CALIBRATION GROUND STATION

Spencer S. Haycock

Department of Electrical and Computer Engineering

Master of Science

The SeaWinds Calibration Ground Station (CGS) is a passive ground station used to receive and sample transmissions from the SeaWinds scatterometer. During post processing, the received transmissions are characterized in order to verify proper instrument operation and to eliminate error in satellite telemetry and in data products generated from processing SeaWinds data. Sources of instrument error include uncertainties in transmitted power, pulse timing, and carrier frequency drift. Identifying these errors prevents their propagation to data products.

A key aspect of this analysis involves accurately estimating the parameters of the SeaWinds transmissions. As better parameter estimates are researched and developed, the scatterometer can be more finely calibrated and better characterized, allowing improved accuracy of environmental measurements. This work explores several methods to estimate SeaWinds frequency parameters by parametrically modeling the signal as a series of linear FM pulses. Improved frequency estimates are obtained by transforming the signal into appropriate signal spaces. These methods are compared and their tradeoffs revealed.

SNR regions are assigned to each method to mark appropriate performance bounds, and improvements over previous SeaWinds data analysis methods are shown. Finally, recent estimates of SeaWinds parameters are disclosed. This analysis helps to advance the level to which future scatterometer instruments may be calibrated, providing the potential for more accurate scatterometer data products.

ACKNOWLEDGMENTS

And if any man think that he knoweth any thing,
he knoweth nothing yet as he ought to know.

1 Corinthians 8:2

This work is dedicated to those who endeavor to be the best at what they do, no matter how challenging the task may be nor how incompetent they may feel. I would like to express my appreciation to my advisor Dr. Long for opening the door to the MERS Lab, providing me with many opportunities to gain valuable experience. I would also like to thank my parents, Scott and Suzanne, for their endless love and support during my college education. Finally, special thanks to JaNae, the love of my life, for her encouragement during the compilation of this work.

Contents

Acknowledgments	xiii
List of Tables	xvii
List of Figures	xx
1 Introduction	1
1.1 Linear FM Parameter Estimation	2
1.2 Previous Research Involving the Calibration Ground Station	2
1.3 Thesis Outline	3
2 Instrument Parameters and Operation	5
2.1 The SeaWinds Scatterometer	5
2.2 The Calibration Ground Station (CGS)	8
2.3 Summary	13
3 Analysis of Linear FM Waveforms	15
3.1 Linear FM Waveforms	16
3.2 Discrete Analytic Signal	17
3.3 Signal-to-Noise Ratio (SNR)	18
3.4 Discrete Fourier Transform (DFT)	19
3.5 Spectrogram ($ \text{STFT} ^2$)	20
3.6 Wigner Distribution (WD)	22
3.7 Radon Transform of the WD	24
3.8 Summary	26

4	Estimation of Linear FM Pulse Parameters	29
4.1	Matched Filtering	29
4.2	Arrival Time Estimation	32
4.3	Frequency Estimation	34
4.3.1	Estimation of Center Frequency by DFT	35
4.3.2	Quadratic Regression on Unwrapped Signal Phase	35
4.3.3	Dechirping Matched Filter Bank	42
4.4	Summary	46
5	Results	47
5.1	Sample Rate Limitations	47
5.2	Initial Estimates	48
5.3	Separation of Doppler Compensation and Doppler Shift	48
5.4	Comparison of Estimation Methods Used by the Doppler Model	51
5.5	Evaluation of SeaWinds Performance over Time	58
5.6	Summary	65
6	Conclusion	67
A	CGS Maintenance and Installation	71
	Bibliography	74

List of Tables

2.1	Key SeaWinds Parameters (Nominal)	7
2.2	Parameters Normalized by Sample Rate (A/D Conversion)	12
5.1	Comparison of SeaWinds Performance over Time using CGS Data Sets	58

List of Figures

2.1	Ground track of the SeaWinds scatterometer	6
2.2	Receiver of the SeaWinds Calibration Ground Station.	8
2.3	SeaWinds pulses captured by the CGS	9
2.4	Simplified frequency plan of the CGS receiver	10
2.5	Spectrum aliasing from undersampling in the CGS A/D converter	11
3.1	DFT magnitude of a high-SNR SeaWinds pulse.	21
3.2	Spectrogram of the region surrounding the leading edge of a high-SNR SeaWinds pulse	23
3.3	Discrete-Time Wigner Distribution (DTWD) of the leading edge of a high- SNR SeaWinds pulse	25
3.4	Integration path of the Radon transform.	27
4.1	Output of a filter matched to a SeaWinds pulse	30
4.2	Trailing edges of SeaWinds pulses	33
4.3	Monte Carlo simulation of arrival time estimation by envelope detection	34
4.4	DFT method of estimating pulse center frequency f_0	36
4.5	Monte Carlo simulation of center frequency estimation using the DFT method	37
4.6	Unwrapped phase of a high-SNR SeaWinds pulse	38
4.7	Monte Carlo simulation of chirp rate and center frequency estimates using quadratic regression on unwrapped phase	40
4.8	Monte Carlo simulation of quadratic regression on zero crossings	41
4.9	Output of dechirping matched filter bank	44
4.10	Monte Carlo simulation of chirp rate and frequency estimates using the dechirping matched filter bank method	45

5.1	SNR, chirp rate, and center frequency estimates during an approach of SeaWinds' outer beam	49
5.2	Simplified geometry of the SeaWinds scatterometer and the CGS during a flyby	50
5.3	Number of pulses in a 10-s capture considered in the Doppler model as a function of SNR threshold	52
5.4	Results of performing the DFT method on SeaWinds pulses	53
5.5	Results of performing the phase regression method on SeaWinds pulses	54
5.6	Results of performing the dechirping matched filter bank method on SeaWinds pulses	55
5.7	Standard deviation of center frequency estimates from the Doppler model as a function of SNR threshold	56
5.8	Doppler compensation and Doppler shift estimates as a function of SNR threshold	57
5.9	Outer beam approaching and receding from the CGS in September 2002.	59
5.10	Inner beam approaching and receding from the CGS in September 2002.	60
5.11	Outer beam approaching and receding from the CGS in January 2003	61
5.12	Inner beam approaching and receding from the CGS in January 2003	62
5.13	Outer beam approaching and receding from the CGS in July 2004	63
5.14	Inner beam approaching and receding from the CGS in July 2004	64
A.1	Elevation angles of significant mountains in Utah County	72
A.2	Nick Williams, a BYU Civil Engineering Student, surveys Y Mountain to measure the elevation angle of its summit	73

Chapter 1

Introduction

A scatterometer is an orbiting radar that allows scientists to study the Earth's environment on a global scale by measuring the normalized radar cross section (RCS) of the Earth's surface. Since the RCS of the ocean is a function of surface roughness caused primarily by wind-generated waves, wind speed and direction can be inferred from the RCS. Scatterometers can be used to measure properties of both the atmosphere and the Earth's surface, allowing study of environmental dynamics on a global scale not previously possible. For example, scatterometers can measure wind velocity to understand weather patterns and detect climatic changes, track polar sea ice, and estimate surface moisture to detect drought or deforestation. In order to produce accurate measurements of these environmental factors, the scatterometer must be precisely calibrated.

The SeaWinds scatterometer is onboard the QuikSCAT satellite, launched in June 1999. To assist in calibrating the instrument and to verify proper operation, the Calibration Ground Station (CGS) was developed by NASA Jet Propulsion Laboratory (JPL). The CGS is a passive receiving station that samples and stores the SeaWinds transmissions, allowing passive measurement of the signal characteristics in post processing. Parameters of the SeaWinds transmissions are extracted, examined, and compared to nominal values. Deviations from nominal parameters may then be reported and accounted for in data products generated from SeaWinds RCS data. Independent characterization of these transmissions allows JPL the opportunity to verify correct operation of the SeaWinds scatterometer, increasing the validity of their environmental measurements.

1.1 Linear FM Parameter Estimation

During each scatterometer flyby over the Provo area, the CGS is illuminated for several brief intervals called sweeps that occur when the CGS is illuminated by the main lobe of the SeaWinds beam. During these sweeps, SeaWinds pulses emerge from the noise floor, creating a high-SNR region where key signal parameters may be extracted. Previous signal estimates have only been performed over these high-SNR regions. However, sweeps make up only a small portion of the signal sampled by the CGS, excluding the majority of the data collected by the ground station.

Several methods have been established to estimate the center frequencies of pulses encountered in SeaWinds sweeps. These methods were chosen for their computational efficiency. However, these methods are suboptimal and perform poorly at low SNR. The suboptimality of these methods limits the window over which SeaWinds parameters may be observed.

In this thesis I present methods to blindly and independently estimate the parameters of linear FM pulses received by the CGS, with emphasis on improving center frequency estimates, especially at low SNR. I analyze the established methods and introduce a new method that is statistically optimum, yet computationally intensive. This optimality is obtained by parametrically modeling the SeaWinds signal as a series of linear FM pulses. This significantly increases the observation window of SeaWinds transmissions, allowing the tracking of center frequencies over time. This allows the SeaWinds Doppler compensation algorithm and the Doppler shift to be examined for deviation from nominal values. This ability is used to determine whether the SeaWinds carrier frequency has drifted over its life cycle.

1.2 Previous Research Involving the Calibration Ground Station

The CGS has been analyzed extensively and proved very useful in developing a new calibration methodology needed to evaluate improved scatterometer designs. Yoho [1] presented new calibration techniques and addressed issues related to new scatterometer designs. These included calibration methodology; parameter separation; calibration of surface location measurement; scatterometer measurement correlation and data variance; and

a comprehensive telemetry-based system simulation model to support the development of scatterometer applications by estimating instrument timing, frequency, position, pointing, and power. Anderson [2] analyzed several aspects of the SeaWinds/CGS system. He performed an orbital geometric analysis to determine Doppler frequency and antenna pattern angles from satellite telemetry; evaluated the sensitivity of the received SeaWinds signal to perturbations in satellite position, altitude, and timing; inspected multipath effects at White Sands, New Mexico; and formulated a method to determine the center frequency of the received SeaWinds signal. Adams [3] characterized the performance and operation of the Calibration Ground Station in a variety of operating conditions, including calibration and testing of the CGS to determine thermal and gain stability.

1.3 Thesis Outline

This thesis is organized as follows. Chapter 2 introduces the SeaWinds scatterometer and the CGS, describes their operation, and reveals important factors that describe the behavior of the signal as it is received by the CGS.

Chapter 3 describes linear FM waveforms and elaborates on the characteristics of the transmitted SeaWinds pulses. A modified discrete analytic signal is introduced to account for undersampling introduced by the CGS. Time-frequency transforms are introduced as ideal signal spaces from which to estimate linear FM parameters. The Radon transform of the Wigner distribution is identified as a maximum likelihood estimator of these parameters.

Chapter 4 analyzes methods to estimate parameters of the SeaWinds pulses. Envelope detection is used to find high-SNR pulses, from which the locations of low-SNR pulses are deduced. Three frequency estimation methods are compared. Their performance is evaluated for accuracy, SNR performance, and computational intensity. A dechirping matched filter bank is identified as an optimal estimator, and is equated to the Radon transform of the Wigner distribution. Since this method is extremely computationally intensive, quadratic regression on unwrapped signal phase can be used at high SNR as a suboptimal algorithm that is computationally more efficient.

Chapter 5 applies these methods to the estimation of real SeaWinds pulses. Doppler compensation and Doppler shift are separated using non-linear least squares regression on a model of these parameters. Three SeaWinds data sets are examined which verify that the SeaWinds instrument is operating correctly.

Chapter 6 concludes this thesis with research contributions and future recommendations.

Chapter 2

Instrument Parameters and Operation

The SeaWinds scatterometer and the Calibration Ground Station form a one-way system designed to verify proper operation of the SeaWinds instrument. In this chapter, details of SeaWinds scatterometer operation are revealed and the parameters of its transmitted signal are identified. The process of capturing SeaWinds transmissions by the Calibration Ground Station is shown, including its frequency plan and the details associated with under-sampling the downmixed signal. Knowledge of this system is paramount to understanding the behavior of the received signal, allowing proper estimation of its parameters.

2.1 The SeaWinds Scatterometer

The SeaWinds scatterometer is located onboard the QuikSCAT satellite in an 803-km sun-synchronous low earth orbit (LEO). The scatterometer transmits electromagnetic pulses to the Earth's surface, from which the backscatter is received and observed, in order to indirectly obtain environmental measurements. QuikSCAT's orbit allows SeaWinds to illuminate more than 90% of the Earth's surface in 24 hours, usually passing twice daily over Provo, Utah.

Nominal SeaWinds parameters are listed in Table 2.1. SeaWinds transmits linear FM pulses at a 13.402-GHz carrier frequency. This value was chosen because frequencies near 13.4 GHz are “sensitive to capillary waves on the ocean surface induced by local winds” [4]. The pulses are transmitted from two alternating antenna beams (Fig. 2.1). The outer beam is elevated 46° from nadir and transmits vertically polarized pulses; the inner beam is elevated at 40° and is horizontally polarized [4]. The nominal 1.5-ms pulse width and 5.4-ms pulse repetition interval (PRI) are based on “spacecraft altitude and antenna

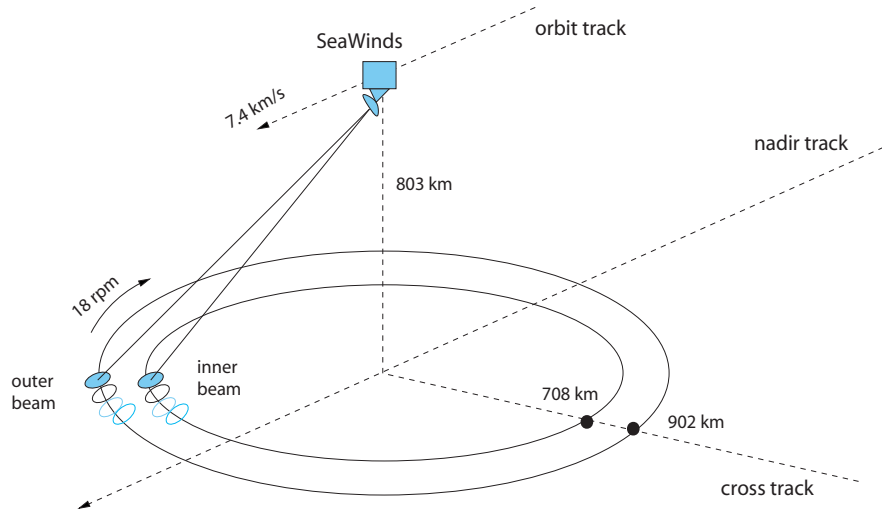


Figure 2.1: Ground track of the SeaWinds scatterometer. Pulses are transmitted from two alternating antenna beams. The rotating dish causes the beams to trace out a helical pattern along the Earth's surface [2].

scanning geometry” and are chosen to eliminate gaps in the scan swath by producing an appropriate beam pattern [4]. Note that since the transmitted pulses successively alternate between the inner and outer beams, the effective PRI of each beam is approximately 10.8 ms.

The antenna rotates at 18 rpm, tracing out a helical pattern on the Earth's surface. As the antenna rotates, the two-way Doppler shift in echoed pulses received by SeaWinds modulates the received center frequency as a cosine of the azimuth angle of the antenna, with amplitude 480 kHz (430 kHz) for the outer beam (inner beam) [4]. Commanded Doppler is used to precompensate the carrier frequency for the Doppler shift anticipated in echoed pulses so that no net Doppler shift (within 10 kHz) results [5]. This allows the SeaWinds receiver to operate with a fixed frequency response intended for the echo returns [4]. In order to account for orbital geometry, the commanded Doppler is formed from a lookup table parameterized by the orbit step and the azimuth angle of the antenna as QuikSCAT traverses its orbit. The commanded Doppler consists of a cosine function with phase, amplitude, and bias parameters for 256 equally-spaced temporal orbit steps [4].

Table 2.1: Nominal SeaWinds Parameters [4] [5]

Parameter	Value
Carrier frequency f_c	13.402 GHz
Chirp rate μ_c	-250.73 MHz/s
Pulse width τ	1.5 ms
Pulse repetition interval (PRI)	5.4 ms
Antenna spin rate	18 rpm
Antenna peak sidelobe	≤ -15 dB
Outer beam	
Nadir angle	46°
3-dB beamwidth	1.4°(el) x 1.7°(az)
Range Delay	8.3 ms
Max. Doppler ν_d observed by CGS	± 240 kHz
Inner Beam	
Nadir angle	40°
3-dB beamwidth	1.6°(el) x 1.8°(az)
Range Delay	7.3 ms
Max. Doppler ν_d observed by CGS	± 215 kHz



Figure 2.2: Receiver of the SeaWinds Calibration Ground Station at BYU, Provo, Utah. Ducting tubes pump cool air into the radome and protect sensitive cables connected to computers below.

2.2 The Calibration Ground Station (CGS)

The CGS (Fig. 2.2) was originally located in White Sands, New Mexico, and was built in order to calibrate the scatterometer onboard the QuikSCAT satellite launched in June 1999. It was acquired by the BYU Microwave Earth Remote Sensing (MERS) Laboratory in March 2002 in order to continue monitoring SeaWinds on QuikSCAT and to observe transmissions from the SeaWinds scatterometer onboard the Advanced Earth Observation Satellite II (ADEOS-II), launched in December 2002. The MERS Lab helped evaluate proper operation of ADEOS-II by measuring parameters of the new SeaWinds scatterometer. However, the ADEOS-II satellite suddenly lost power in October 2003 due to a solar panel malfunction; as a result, only SeaWinds on QuikSCAT is currently observed by the CGS.

The CGS, positioned on the roof of the Clyde Building on BYU campus, continues to regularly receive SeaWinds transmissions. In order to successfully receive a signal, the

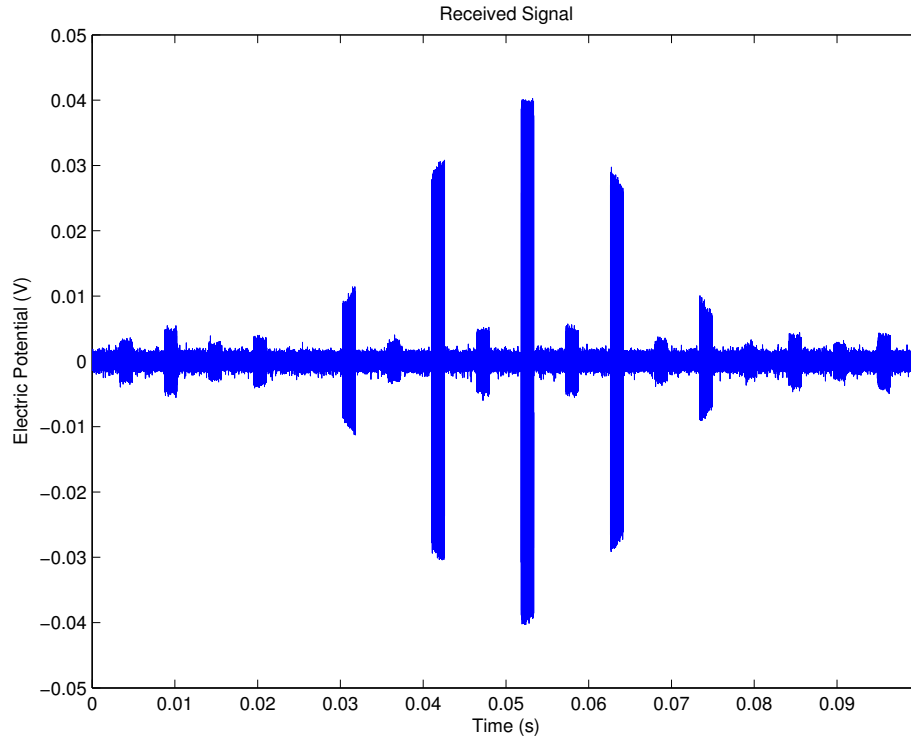


Figure 2.3: SeaWinds pulses captured by the CGS. A 100-ms interval shows the received SeaWinds pulses emerge from the noise floor as the outer beam of SeaWinds sweeps across the main lobe of the CGS receiver during a flyby over Provo, Utah. The pulses transmitted from the inner beam are observed between those of the outer beam and have lower SNR since the main lobe of the inner beam is not pointing directly at the CGS.

computer-controlled pedestal is programmed to point the receiving antenna at SeaWinds during each flyby. The CGS antenna is held fixed during capture of each beam to reduce jitter. Pointing errors resulting from the fixed antenna and the moving satellite can be ignored because the CGS antenna has a wide main lobe. During each flyby, the CGS is illuminated for several brief intervals called sweeps (Fig. 2.3), which occur due to the rotating dish antenna. Since these sweeps yield pulses with relatively high SNR, signal parameters extracted from pulses within these sweeps are more likely to yield accurate estimates than those obtained from other low-SNR regions of the signal.

Usually, only 10 seconds are sampled for each beam that passes over the CGS, yielding 40 seconds of total data per flyby. These captures are separated into manageable 100-ms sections (“`.raw`” files) and stored for offline processing. Each file contains

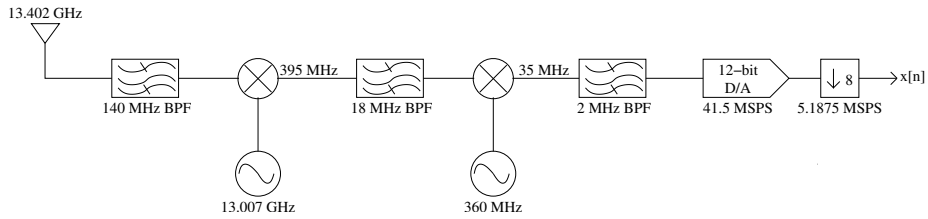


Figure 2.4: Simplified frequency plan of the CGS receiver. The signal is received at 13.402 GHz, mixed down to 35 MHz, sampled at 41.5 MSPS, and decimated by 8, yielding an observed carrier frequency of 3.875 MHz and a sample rate of 5.1875 MSPS.

a 1024-byte header which reveals basic sampling information, including start time, beam description, and first and second-order signal statistics. These files can be linked together to form one large beam capture.

The CGS receiver is a double conversion superheterodyne that consists of two parts: the front end is located in an insulated metal box mounted on the pedestal within the radome, while the rest is cascaded via coaxial cable to the computer racks. The signal is received by a circularly polarized corrugated horn antenna, folded to 35 MHz, sampled at 41.5 MSPS, and decimated by 8 to yield an effective 5.1875 MSPS sample rate (Fig. 2.4). The undersampling in this process leads to aliasing which results in a reversal in the frequency spectrum where the positive spectrum is swapped with the negative spectrum (Fig. 2.5). As a result, the SeaWinds linear FM downchirp is perceived as an upchirp by the CGS. Although a swapped spectrum exists in the sampled data due to aliasing, this can be ignored by simply treating the negative frequency spectrum as if it were positive.

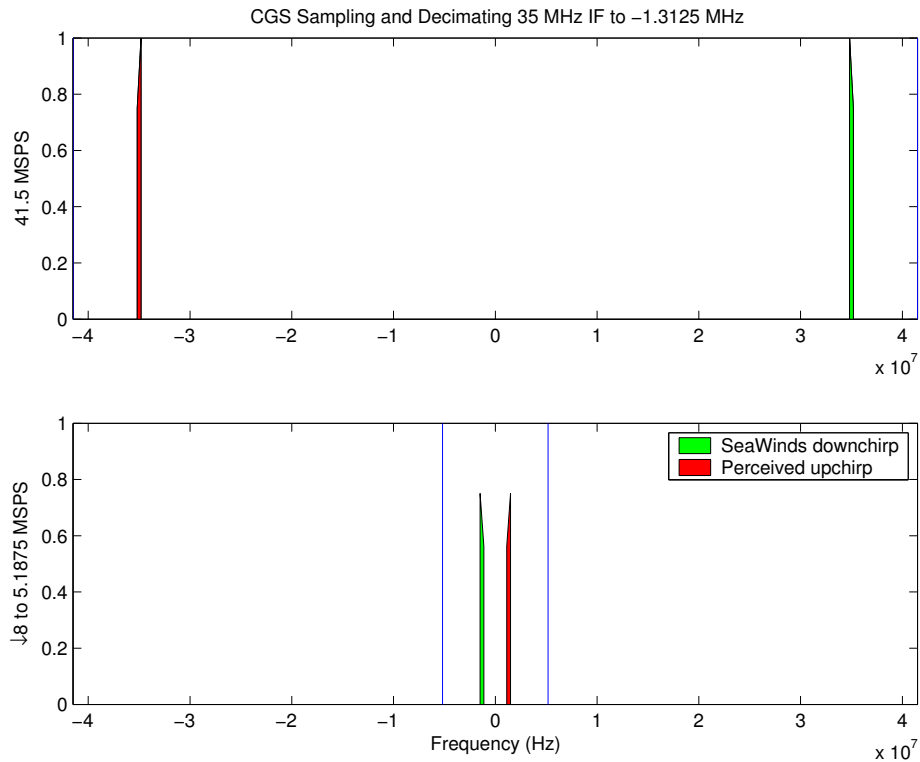


Figure 2.5: Spectrum aliasing from undersampling in the CGS A/D converter. The top plot depicts the received SeaWinds spectrum downmixed to 35 MHz IF. The limits of the plot correspond to the 41.5-MSPS sample rate. The proximity of these two frequencies violates the Nyquist Sampling Theorem. The bottom plot illustrates the consequent aliasing in the frequency spectrum as the signal is undersampled and decimated. The right spectrum is swapped with the left, and the 41.5-MSPS sample rate is reduced to 5.1875 MSPS. However, since no spectral overlap occurs, no signal information is lost to aliasing.

Table 2.2: Parameters Normalized by Sample Rate (A/D Conversion)

$$x(t) = e^{-j2\pi(f_0t + \frac{\mu}{2}t^2)} \longleftrightarrow x[n] = e^{-j2\pi(f_0n + \frac{\mu}{2}n^2)}$$

Parameter	Symbol	Downmixed to 35 MHz IF	Sampled at 5.1875 MSPS
Doppler time compression	α	$\in [0.999982, 1.000018]$	(same)
Max. Doppler compensation	ν_c	480 kHz	$\frac{192}{2075} \approx .092530$
Center frequency (transmit)	$f_c = 13.402 \text{ GHz}$	3.875 MHz	$\frac{62}{83} \approx .746988$
Center frequency (receive)	$f_0 = \alpha [f_c + \nu_c \cos(\phi_c)]$	$\in [3.152, 4.598] \text{ MHz}$	$\in [.607, .887]$
Chirp rate (transmit)	μ_c	-250.73 MHz/s	$-9.31730004355 \times 10^{-6}$
Chirp rate (receive)	$\mu = \alpha^2 [\mu_c - 2\pi \frac{18}{60} \nu_c \sin(\phi_c)]$	$\in [-251.644, -249.816] \text{ MHz/s}$	$\in [-9.351, -9.283] \times 10^{-6}$
Pulse width	τ	1.5 ms	7781.25 samples
PRI	PRI	5.4 ms	28,012.5 samples

2.3 Summary

The operation of the SeaWinds instrument and the Calibration Ground Station have been examined in detail. The rotation of the antenna beams causes SeaWinds to illuminate the CGS in sweeps, limiting the time interval over which signal parameters may be estimated from pulses above the noise floor. In addition, the commanded Doppler compensation algorithm modulates the effective carrier frequency of the transmitted SeaWinds pulses. The CGS receives the Doppler-shifted signal that has been modulated by the Doppler compensation algorithm, the sum of which results in an observed Doppler shift that appears negated. The signal is then downmixed and undersampled at 5.1875 MSPS to an effective 3.875 MHz. Knowledge of these factors is essential to understanding the behavior of the received signal, improving the ability to estimate its parameters. The next chapter addresses ways to model these pulses to obtain accurate parameter estimates.

Chapter 3

Analysis of Linear FM Waveforms

SeaWinds transmits linear FM pulses which are commonly used in pulse-compression radars to achieve high range resolution by increasing the time-bandwidth product of the signal. The greater range resolution is obtained at the output of a filter matched to a pulse-compressed waveform at the receiver [6] [7]. To better estimate parameters of the linear FM waveform, we model the phase of the waveform as a quadratic function of time such that the chirp rate, center frequency, and phase offset are obtained from the coefficients of this function. The phase is obtained by unwrapping the phase of the analytic signal or by finding the zero-crossings of the real signal. Another way to estimate chirp rate and center frequency is by using time-frequency transforms.

Due to its chirped instantaneous frequency, a linear FM waveform is inherently nonstationary. Its analysis requires tracking an evolving signal spectrum. This may be facilitated by using a time-frequency distribution (TFD), which is an energy density function of time and frequency. Since random noise in one dimension tends to spread over the time-frequency plane while signals of interest concentrate their energy over specific time intervals and frequency bands, a TFD is very useful for analyzing signals corrupted by random noise [8] [9]. The basis functions of time-frequency transforms are localized in both time and frequency, providing a better signal space from which to observe nonstationary signals. This can significantly enhance the ability to estimate signal parameters. In this chapter, linear FM waveforms, the discrete analytic signal, and the Discrete Fourier Transform are introduced, followed by discussion of the Spectrogram, the Wigner distribution, and the Radon transform of the Wigner distribution. This information provides the proper background to understand the properties of estimation methods in Chapter 4.

3.1 Linear FM Waveforms

Linear FM waveforms are a subclass of polynomial-phase signals of the form

$$s(t) = \Re \{ A(t)e^{j\phi(t)} \} \quad (3.1)$$

where the phase of order p is defined as

$$\phi(t) = \sum_{i=0}^p a_i t^i. \quad (3.2)$$

The instantaneous frequency (IF) of the waveform is defined by applying a time derivative to the phase and converting from radians to Hz, yielding

$$f(t) \triangleq \frac{1}{2\pi} \frac{d}{dt} \phi(t) = \frac{1}{2\pi} \sum_{i=1}^p i a_i t^{i-1}. \quad (3.3)$$

Likewise, the instantaneous chirp rate is obtained by applying a time derivative to the IF,

$$\mu(t) \triangleq \frac{d}{dt} f(t) = \frac{1}{2\pi} \sum_{i=2}^p i(i-1) a_i t^{i-2}. \quad (3.4)$$

The phase $\phi(t)$ of a linear FM pulse is quadratic,

$$\phi(t) = 2\pi \left(f_0 t + \frac{\mu}{2} t^2 \right) + \phi_0, \quad -\frac{\tau}{2} \leq t \leq \frac{\tau}{2} \quad (3.5)$$

with chirp rate μ (Hz/s), center frequency f_0 (Hz), and phase offset ϕ_0 (rad) defined at the temporal center $t = 0$ of a pulse of length τ . Applying Eq. 3.3 to Eq. 3.5, the instantaneous frequency $f(t) = f_0 + \mu t$ is swept linearly in time. Since SeaWinds adds a sinusoidally-varying Doppler compensation bias to the carrier frequency, the phase of the transmitted SeaWinds pulse is modeled as

$$\phi(t) = 2\pi \left[f_c + \nu_c \cos\left(2\pi \frac{18}{60} t + \phi_c\right) + \frac{\mu_c}{2} t \right] t + \phi_0, \quad -\frac{\tau}{2} \leq t \leq \frac{\tau}{2}, \quad (3.6)$$

where f_c is the SeaWinds carrier frequency, ν_c and ϕ_c are the amplitude and phase offset of the commanded Doppler, and μ_c is the nominal SeaWinds chirp rate. Since the CGS receives the transmitted waveform modulated by the Doppler effect, the phase of the received waveform is modeled as that of the transmitted waveform whose time axis is scaled by the compression factor α [10]:

$$\phi(\alpha t) = 2\pi \left[f_c + \nu_c \cos\left(2\pi \frac{18}{60} \alpha t + \phi_c\right) + \frac{\mu_c}{2} \alpha t \right] \alpha t + \phi_0, \quad -\frac{\tau}{2} \leq t \leq \frac{\tau}{2} \quad (3.7)$$

where $\alpha = 1 + \frac{v}{c}$ is assumed constant over each pulse, with v being the relative velocity of an approaching target and c the speed of propagation. The SeaWinds pulse is modeled as [11]

$$x(t) = \sqrt{\alpha}A(\alpha t)e^{j\phi(\alpha t)} + \eta(t), \quad (3.8)$$

where $A(t)$ is the signal magnitude and $\eta(t)$ is complex white Gaussian noise. Using Eq. 3.7, it can be shown that the parameters we wish to estimate at the temporal center of each pulse are

$$\begin{aligned} \mu &= \alpha^2 \left[\mu_c - 2\pi \frac{18}{60} \nu_c \sin(\phi_c) \right] \in [-251.644, -249.816] \text{ MHz/s} \\ f_0 &= \alpha [f_c + \nu_c \cos(\phi_c)] \in 13.402 \text{ GHz} + [-723, 723] \text{ kHz} \\ \phi_0 &= \phi_0 \in [-\pi, \pi] \text{ rad.} \end{aligned} \quad (3.9)$$

3.2 Discrete Analytic Signal

The signal $x(t)$ of Eq. 3.8 is the complex equivalent of the real signal received by the CGS. The complex representation is commonly used to obtain the signal phase and amplitude [12]. However, since the CGS samples the received signal, a discrete-time version of Eq. 3.8 must be formulated. Let

$$s[n] = A[n]e^{j\phi[n]}, \quad 0 \leq n \leq N - 1 \quad (3.10)$$

$$x[n] = s[n] + \eta[n], \quad 0 \leq n \leq N - 1, \quad (3.11)$$

where $s[n]$ is the complex signal and $\eta[n]$ is a realization of zero-mean complex white Gaussian noise with variance σ_η^2 . For simplicity, the time compression factor α is absorbed into the magnitude and phase of Eq. 3.10.

The imaginary part of the complex signal is formed by shifting the phase of the real signal by 90° (quadrature method), or by forming the discrete analytic signal. An analytic signal is defined as a signal without negative frequency components. True analytic signals do not exist in discrete time; however, we call the discrete-time equivalent the discrete analytic signal, or simply the analytic signal (in context). Two important properties of the analytic signal are that the real part is equal to the original discrete-time sequence, and the real and imaginary parts are orthogonal over the finite interval. To satisfy these constraints, the positive spectrum is doubled and the negative spectrum is eliminated by forcing it to

zero. Since the discrete-time spectrum is periodic, we actually create a one-sided periodic spectrum.

Recall that the CGS causes a reversal in the frequency spectrum. To use the correct spectrum for estimation, we introduce a modified discrete analytic signal that discards the positive spectrum as opposed to the negative spectrum. Assuming N is even, the discrete-time analytic signal is computed by performing a DFT (Sec. 3.4), modifying the spectrum as [13]

$$X'[k] = \begin{cases} X[0], & k = 0 \\ 0, & 1 \leq k \leq \frac{N}{2} - 1 \\ X[\frac{N}{2}], & k = \frac{N}{2} \\ 2X[k], & \frac{N}{2} + 1 \leq k \leq N - 1 \end{cases} \quad (3.12)$$

and then performing an inverse DFT. This complex signal reveals the signal amplitude and phase, which can be used to estimate signal parameters. For example, at sufficient SNR quadratic regression on the unwrapped phase $\phi[n]$ reveals estimates of chirp rate, center frequency, and phase offset of the waveform.

3.3 Signal-to-Noise Ratio (SNR)

SeaWinds pulses are received by the CGS at various SNR depending on the alignment of the SeaWinds and CGS antenna beams. The SNR is determined by the received signal power, the noise figure, and the receiver bandwidth [8]. Since SNR affects the accuracy of parameter estimation, it is desirable to discriminate high-SNR pulses from those of low SNR. To calculate average or instantaneous SNR, an estimate of the ambient noise power σ_η^2 in the captured data must first be obtained by sample averaging the power of $x[n]$ over the intervals between pulses, where $s[n] = 0$. This yields

$$\hat{\sigma}_\eta^2 = \frac{1}{N} \sum_{n=0}^{N-1} \eta[n] \eta^*[n]. \quad (3.13)$$

To obtain the average SNR for each pulse, the average signal power is divided by σ_η^2 . The average signal power E_s/N is the signal energy $E_s = \sum_{n=0}^{N-1} s[n]$ divided by the length N

of the signal. It is first obtained by expanding the average received power E_x/N :

$$\frac{E_x}{N} = \frac{1}{N} \sum_{n=0}^{N-1} (s[n]s^*[n] + \underbrace{\eta[n]s^*[n] + s[n]\eta^*[n] + \eta[n]\eta^*[n]}_{\approx 0}) \quad (3.14)$$

$$= \frac{1}{N} \sum_{n=0}^{N-1} |s[n]|^2 + \frac{1}{N} \sum_{n=0}^{N-1} |\eta[n]|^2 = E_s/N + \hat{\sigma}_\eta^2. \quad (3.15)$$

This results in the average SNR

$$SNR_{avg} = \frac{E_s/N}{\hat{\sigma}_\eta^2} = \frac{E_x/N - \hat{\sigma}_\eta^2}{\hat{\sigma}_\eta^2}. \quad (3.16)$$

The instantaneous SNR at time n is simply the signal power divided by the noise power:

$$\frac{|s[n]|^2}{\sigma_\eta^2}. \quad (3.17)$$

SNR can also be given an alternative definition in different signal spaces, where the SNR is only defined over the time-frequency region in which the signal resides [9]. For example, a low-SNR signal that is buried in noise in the time domain may be transformed into the frequency domain to reveal an identifiable tone. The SNR defined over the bandwidth of the signal in the frequency domain is then higher than that observed in the time domain since the bandwidth over which the SNR applies is narrowed. Likewise, as the signal is transformed into the time-frequency plane, the SNR defined over the narrow time-frequency region in which the signal resides is higher than the SNR defined over the entire time-frequency plane. Our goal is to choose the signal space that maximizes the SNR over the time-frequency region in which the signal resides, and then perform parameter estimation of the signal within that space.

3.4 Discrete Fourier Transform (DFT)

Let a set of K waveforms defined on the interval $0 \leq n \leq N - 1$ form the basis $\mathcal{B} = \{\phi_0[n], \phi_1[n], \dots, \phi_{K-1}[n]\}$ of a signal space. If we project the signal $x[n]$ onto each of the basis functions $\phi_k[n]$, we arrive at the signal space projection $X[k] = \langle x[n], \phi_k[n] \rangle$, or the analysis equation

$$X[k] = \sum_{n=0}^{N-1} x[n]\phi_k^*[n] = \boldsymbol{\phi}_k^H \mathbf{x}. \quad (3.18)$$

If we define the basis functions as $\phi_k[n] = \frac{1}{\sqrt{N}}e^{j2\pi\frac{k}{N}n}$, we can construct an orthonormal basis of complex exponentials equally spaced in frequency. The analysis equation then becomes the unitary Discrete Fourier Transform (DFT)

$$X[k] = \frac{1}{\sqrt{N}} \sum_{n=0}^{N-1} x[n]e^{-j2\pi\frac{k}{N}n}, \quad (3.19)$$

where k is the frequency bin index. Thus, we project a band-limited discrete-time signal (an expansion of shifted sinc functions) onto a basis of complex exponentials. The spectrum (Fig. 3.1) reveals no information as to when these frequencies occur in time: the time-changing signal spectrum is embedded in the phase of the DFT. Although this signal space allows estimation of the signal bandwidth, it is difficult to track the instantaneous frequency as it changes over time. However, this can be accomplished using time-frequency transforms.

3.5 Spectrogram ($|\text{STFT}|^2$)

Since complex exponentials are constant-frequency functions that are infinite in duration, a basis set of these functions cannot model a time-changing signal spectrum. One solution to this problem is to window the input signal so that only a portion of the signal is observed, allowing estimation of the signal spectrum over short time intervals. This imposes a piecewise stationary model of the data [14]. The discrete-time Short-Time Fourier Transform (STFT) is defined as [15]

$$X[n, k] = \sum_{m=0}^{L-1} x[n+m]w[m]e^{-j2\pi\frac{k}{N}m}, \quad 0 \leq n, k \leq N-1, \quad (3.20)$$

which is the DFT of the windowed signal. The STFT is a modification of the DFT which provides time resolution at the expense of frequency resolution. The sliding window of length L limits the interval over which the DFT is taken, effectively dividing the signal into time segments so that a changing signal spectrum is observed. It can be interpreted as the projection of the signal onto a basis set whose waveforms are of finite time duration [8].

The squared STFT results in the spectrogram, a plot of signal energy over the time-frequency plane. Although one of the most widely known TFDs, the spectrogram has disadvantages such as a lack of finite support (Fig. 3.2) and the inherent tradeoff between

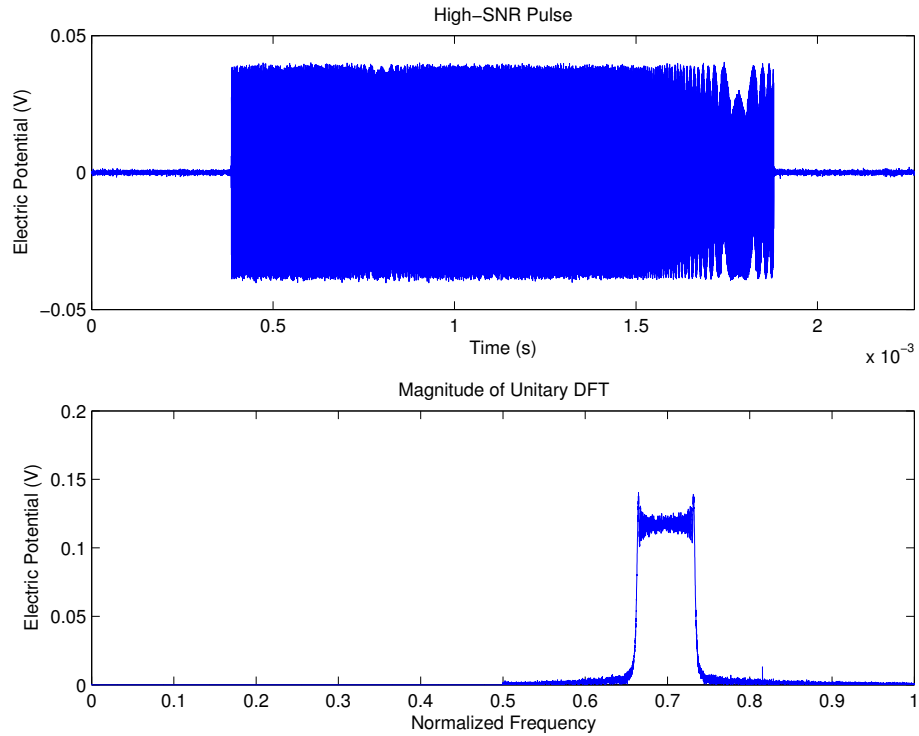


Figure 3.1: DFT magnitude of a high-SNR SeaWinds pulse generated from the modified analytic signal. The top plot shows the received pulse; the bottom reveals the DFT magnitude. The modified analytic signal eliminates the lower half $(0, 0.5)$ of the spectrum without losing information since the spectrum is conjugate symmetric for real signals. Note that the spectrum reveals the frequencies in the time interval over which the DFT is taken, but no information is given as to when these frequencies occur within this interval; the time-changing spectrum is not readily observable from the DFT.

time and frequency localization due to the window function [12]. To balance time and frequency resolution, it can be shown that the optimal length of a rectangular window for a monocomponent signal of constant amplitude is [16]

$$T_w = \sqrt{2} \left| \frac{df(t)}{dt} \right|^{-1/2}, \quad (3.21)$$

where $f(t)$ is the signal IF. This minimizes the -3dB width of the ridge in the time-frequency plane. For linear FM signals, this reduces to [16]

$$T_w = \sqrt{2\tau/B}, \quad (3.22)$$

where τ is the pulse width and B is the pulse bandwidth. Using the nominal values in Table 2.1, we have $T_w = 89.3\mu s$, or $L = 463$ samples. Although the lack of finite support is noted, the STFT performs reasonably in resolving the chirped signal and displaying the frequency spectrum as a function of time.

3.6 Wigner Distribution (WD)

The disadvantages of the STFT warrant the pursuit of other time-frequency transforms. The Wigner distribution (WD) is a popular TFD well-known for its high resolution and properties that are convenient to linear FM waveforms. The Wigner Distribution of the analytic signal is known as the Wigner-Ville distribution. The WD is a joint time-frequency energy distribution based on the marginal conditions [12] [16]. These properties simply state that integrating the TFD with respect to time results in the power spectrum $|X(f)|^2$, while integrating with respect to frequency yields the instantaneous power $|x(t)|^2$. Since a window is not used in the WD, its resolution is not impeded by the limitations introduced by a window function [17]. As a result, no tradeoff exists between time resolution and frequency resolution inherent in “short-time” transforms [18]. The WD is designed to handle monocomponent signals; if multicomponent signals are introduced, cross-term interference occurs. However, since the SeaWinds scatterometer transmits a monocomponent signal, this is not a concern. The WD is defined as

$$W_x(t, f) = \int_{-\infty}^{\infty} x\left(t + \frac{\tau}{2}\right)x^*\left(t - \frac{\tau}{2}\right)e^{-j2\pi f\tau} d\tau, \quad (3.23)$$

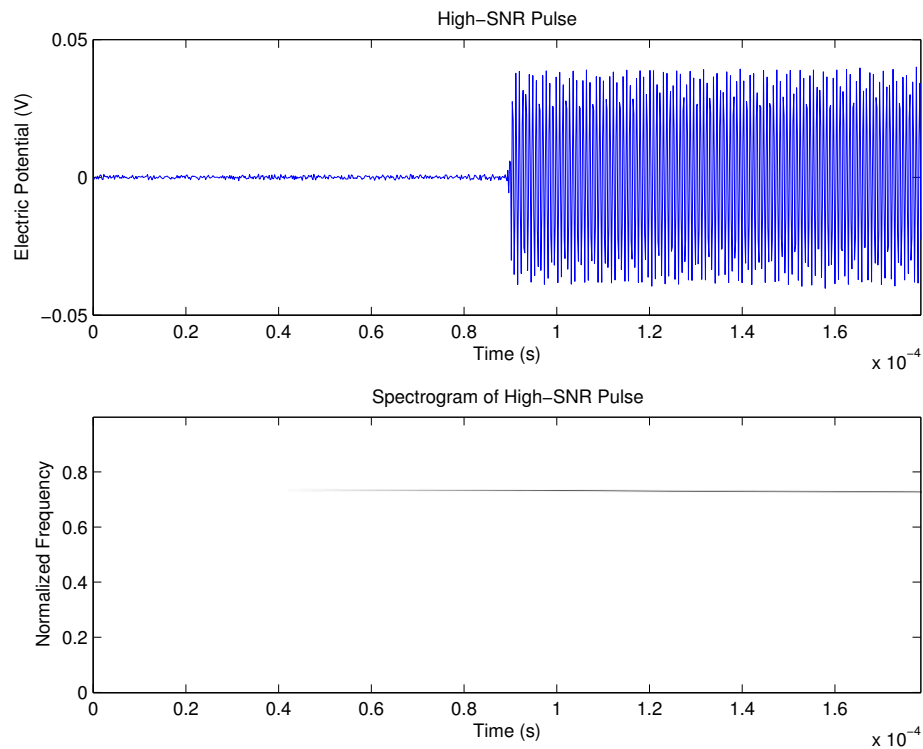


Figure 3.2: Spectrogram of the region surrounding the leading edge of a high-SNR Sea-Winds pulse. The top plot shows the temporal region around the pulse's leading edge; the bottom plot is the Spectrogram of this region using an $89.3\text{-}\mu\text{s}$ window. The Spectrogram is essentially the squared magnitude of the DFT of this window as it slides in time. Due to the window, frequency localization is achieved at the cost of time localization, rendering the beginning of the pulse irresolvable (lack of finite support). However, the instantaneous frequency of the linear FM waveform is clearly observed. Note how random noise essentially disappears by spreading over the time-frequency plane.

which is the Fourier transform of the instantaneous autocorrelation function (IAF) [16]

$$R_x(t, \tau) = x\left(t + \frac{\tau}{2}\right)x^*\left(t - \frac{\tau}{2}\right). \quad (3.24)$$

The IAF is the signal kernel of the WD and is derived such that a unit-amplitude monocomponent signal yields a “knife-edge” delta function that tracks the instantaneous frequency over time. To accomplish this, the kernel of the WD can be derived heuristically, explaining that the Fourier transform of the signal kernel $R_x(t, \tau)$ should yield the “knife edge” $\delta(f - f(t))$. Therefore,

$$R_x(t, \tau) = \mathcal{F}^{-1}\{\delta(f - f(t))\} = e^{j2\pi f(t)\tau} = e^{j\phi'(t)\tau}. \quad (3.25)$$

Since $\phi'(t)$ is obtained in continuous time by taking the derivative of $\phi(t)$, the central finite-difference (CFD) approximation

$$\phi'(t) \approx \frac{1}{\tau} \left[\phi\left(t + \frac{\tau}{2}\right) - \phi\left(t - \frac{\tau}{2}\right) \right], \quad (3.26)$$

which is unbiased for linear FM signals, is used in discrete time. Substituting the CFD into the signal kernel, and assuming a complex unit-amplitude monocomponent signal $x(t) = e^{j\phi(t)}$ we have [12] [16]

$$R_x(t, \tau) = e^{j\phi\left(t + \frac{\tau}{2}\right)} e^{-j\phi\left(t - \frac{\tau}{2}\right)} \quad (3.27)$$

$$= x\left(t + \frac{\tau}{2}\right)x^*\left(t - \frac{\tau}{2}\right). \quad (3.28)$$

Attempts to create discrete-time versions of the Wigner Distribution have resulted in implementations that suffer from inherent aliasing problems. To overcome aliasing, the signal must be sampled at twice the Nyquist rate or the discrete analytic signal must be used. A popular discrete-time implementation is the Discrete-Time Wigner Distribution (DTWD)

$$W_x[n, k] = 2 \sum_m x(n+m)x^*(n-m)e^{-j4\pi \frac{k}{N}m} \quad (3.29)$$

shown in Fig. 3.3.

3.7 Radon Transform of the WD

Since the WD is a density function of signal energy over the time-frequency plane, integrating along all lines in the WD yields the maximum likelihood (ML) estimates of

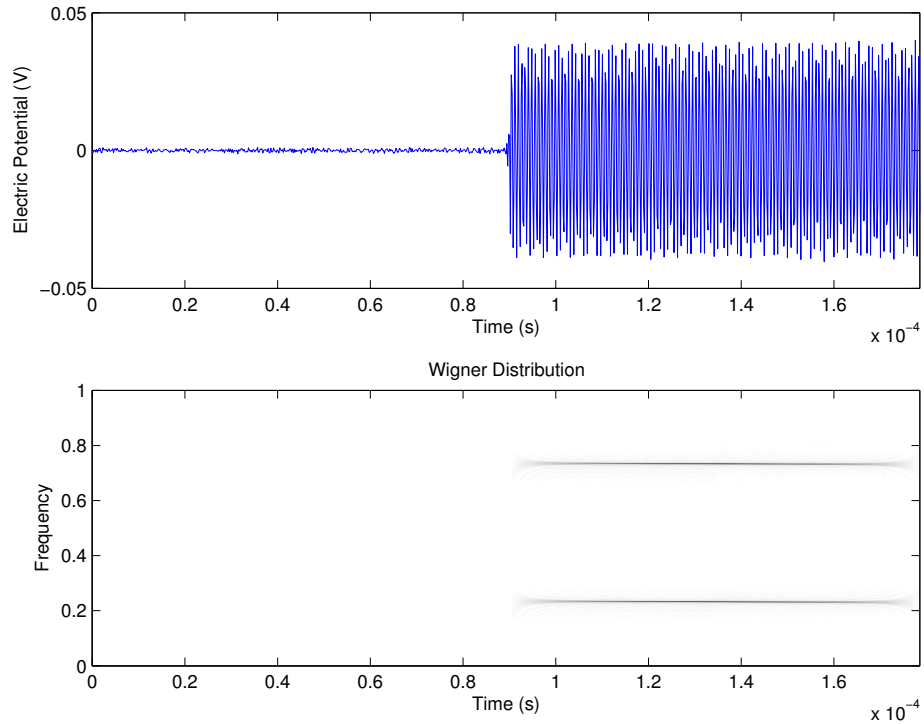


Figure 3.3: Discrete-Time Wigner Distribution (DTWD) of the leading edge of a high-SNR SeaWinds pulse. The top plot shows the same temporal region found in Fig. 3.2 around the pulse's leading edge; the bottom plot is the DTWD of this region. The instantaneous frequency of the signal is clearly visible, although the presence of a mirrored spectrum is noted. The finite support of the transform clearly overcomes the temporal resolution deficiencies of the Spectrogram. Note how random noise also spreads over the time-frequency plane.

linear FM signal parameters in white Gaussian noise [18] [19]:

$$(\hat{\mu}, \hat{f})_{ML} = \arg \max_{\mu, f_0} \int W_x(t, \mu t + f) dt. \quad (3.30)$$

This is equated to the Radon transform of the WD by substituting $\mu = -\cot(\theta)/2\pi$ and $f_0 = r/2\pi \sin(\theta)$, which slices the WD at angle $\theta = \arctan(\frac{-1}{2\pi\mu})$, and scales the projection axis r by $\frac{1}{2\pi \sin(\theta)}$ [19].

The Radon transform $g(r, \theta)$ is the integral of a two-dimensional function $f(x, y)$ over the line interval p , which is parameterized by the perpendicular distance r from the origin and inclination angle θ from the x -axis [20]. Lines in $f(x, y)$ are mapped to points in the Radon space (r, θ) . Creating the rotated coordinate system (r, s) , where $r = x \cos \theta + y \sin \theta$ and $s = -x \sin \theta + y \cos \theta$, the Radon transform of $f(x, y)$ is [20]

$$g(r, \theta) = \int_{-\infty}^{\infty} f(r \cos \theta - s \sin \theta, r \sin \theta + s \cos \theta) ds, \quad -\infty < r < \infty, 0 \leq \theta < \pi \quad (3.31)$$

where r and s are the x and y axes rotated counterclockwise by θ radians (Fig. 3.4) [19].

Restriction of the line integration to specific regions [18] of support in the time-frequency plane can dramatically alleviate computational cost of detecting or estimating the parameters of linear FM waveforms. The region of support for SeaWinds parameters μ and f_0 can be determined from Table 2.2. Note that the received center frequency f_0 cannot change more than 5 kHz per PRI, which narrows the region of support on a pulse-to-pulse basis. However, this optimization is highly dependent on accurately estimating the parameters of the previous pulse, which is not always the case.

A convenient property of the Radon Transform of the WD is that it can be efficiently implemented via a dechirping algorithm that does not require the direct calculation of the WD [19] [21]. This is discussed in Sec. 4.3.3.

3.8 Summary

This chapter has introduced linear FM waveforms, the discrete analytic signal, and several signal transforms. Since time-frequency transforms spread random noise over the time-frequency plane, the effective SNR is increased, improving the potential accuracy of

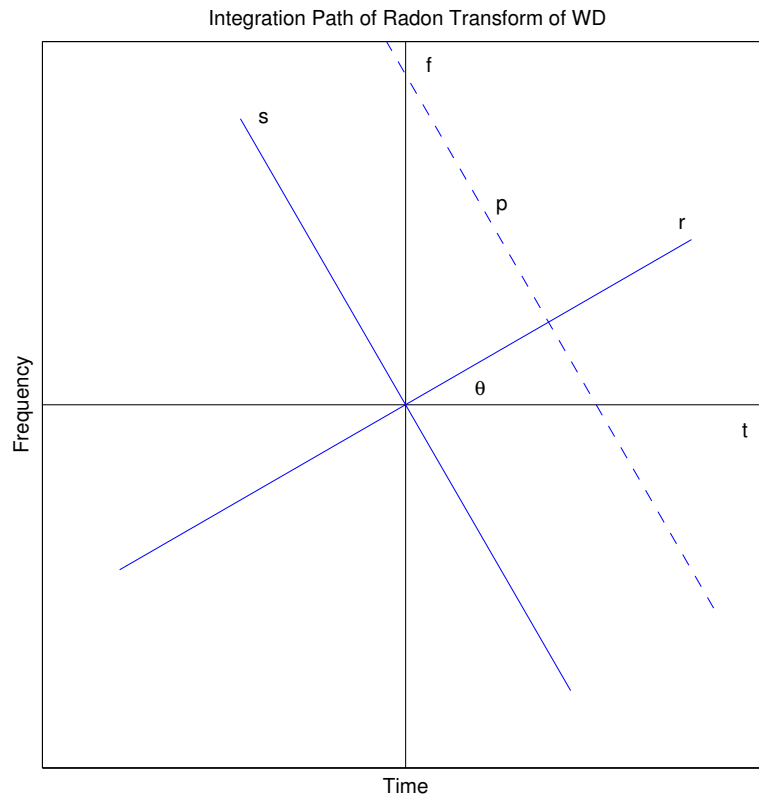


Figure 3.4: Integration path of the Radon transform. All lines of integration p in the time-frequency plane may be specified through parameters r and θ . When applied to the Wigner distribution, the Radon transform becomes a maximum likelihood estimator of the parameters of linear FM signals corrupted by white Gaussian noise.

parameter estimates. In fact, the Radon transform of the WD is a maximum likelihood estimator of linear FM waveform parameters. With this knowledge we are ready to introduce methods of estimating the parameters of linear FM pulses.

Chapter 4

Estimation of Linear FM Pulse Parameters

This chapter describes the theory and limitations of estimation methods for linear FM waveforms. Before frequency estimates can be performed, pulses must be located by estimating their arrival times. This can be done by envelope detection. Once their temporal locations are found, frequency estimation methods are performed over the width of the pulse. Three frequency estimation methods include center frequency estimation by DFT, quadratic regression on unwrapped signal phase, and a dechirping matched filter bank which is equivalent to the Radon transform of the WD. These methods are unique in terms of number of parameters estimated, computational intensity, and SNR performance.

4.1 Matched Filtering

A matched filter correlates a received signal with a signal we wish to detect (Fig. 4.1), providing the maximum possible output SNR when the received signal is corrupted by white Gaussian noise [8]. Although computationally intensive, iterative matched filter banks can locate the leading and trailing edges of each pulse, estimate the frequency content, and determine the total pulse power [22]. In addition, using a quadrature matched filter, as opposed to an incoherent one, can increase the output SNR by 6 dB.

The matched filter can be viewed as the projection of a received signal onto a known basis signal ϕ_0 , where the signal $x[n]$ is convolved with the finite impulse response (FIR) filter $h[n] = \phi_0[N - 1 - n]$, which is the time-reversal of the basis signal we are trying to match. This results in the output convolution sum

$$X[k] = \sum_{n=0}^{N-1} x[n]h[k-n] = \sum_{n=0}^{N-1} x[n]\phi_0^*[N-1-(k-n)] = \sum_{n=0}^{N-1} x[n]\phi_k^*[n], \quad (4.1)$$

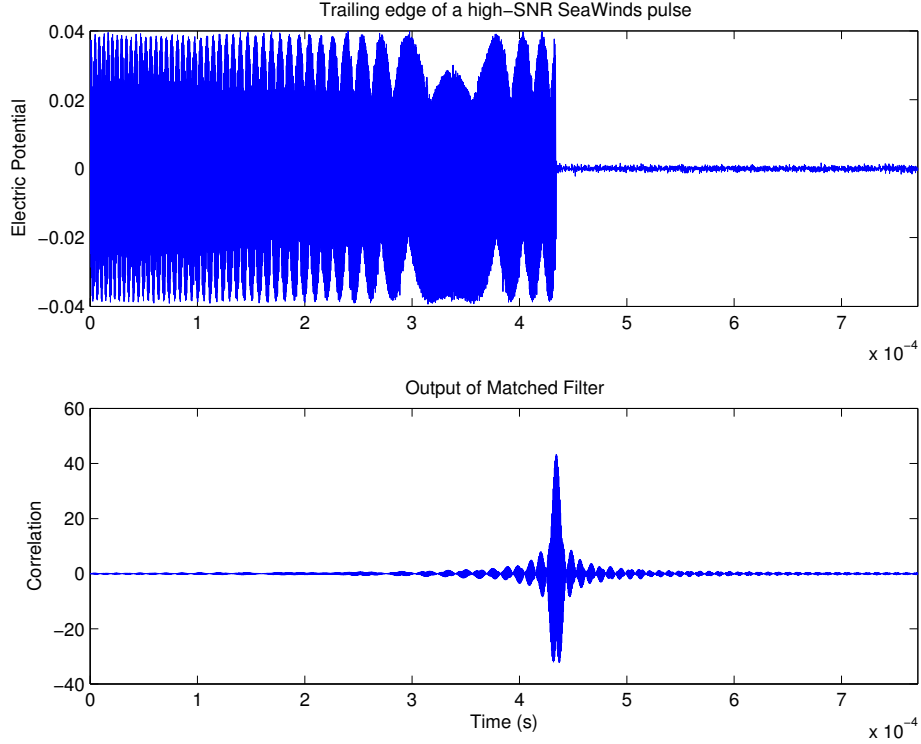


Figure 4.1: Output of a filter matched to a SeaWinds pulse. The top plot reveals the trailing edge of a high-SNR SeaWinds pulse; the bottom plot shows the output of the matched filter, which is the correlation of the filter waveform and the received signal as a function of time. The best match between the filter and the received signal occurs at the peak of the main lobe in the matched filter output, where maximum correlation occurs. This peak occurs at the trailing edge of the SeaWinds pulse. Negative correlation values occur when the phase of the filter and the signal are mismatched.

where $\phi_k^*[n] = \phi_0^*[N - 1 + n - k]$. The output of the filter at index $k = N - 1$ is

$$X[N - 1] = \sum_{n=0}^{N-1} x[n]\phi_0^*[n], \quad (4.2)$$

which is the cross correlation of $x[n]$ and $\phi_0[n]$ [8] [23]. When the filter is matched to the signal such that $x[n] = \phi_0[n]$, the output reaches its peak at $\frac{2E_s}{\sigma_\eta^2}$, which is simply a function of the energy in the signal and does not depend on the waveform itself [11].

The matched filter requires *a priori* knowledge of the transmitted waveform; otherwise, the filter will not provide an optimal output SNR. Hence, its purpose is not intended to measure signal parameters, but to detect known signals. However, estimation may be implemented by using a bank of matched filters over a range of signal parameters and

choosing the output which yields the highest match. The corresponding filter parameters are the parameter estimates.

The output of a filter that is mismatched by a Doppler shift in the received linear FM signal contains a time shift and broadening of the main peak, loss of SNR, and an increase in nearby sidelobes [6]. This is caused by the Doppler effect, which moves part of the signal spectrum outside of the passband of the matched filter [7]. The Woodward ambiguity function is a tool designed to aid engineers in minimizing these effects. It is a joint time-frequency correlation function that is essentially a matched filter bank where the known signal is parameterized by time delay τ and Doppler shift ν . It is used to determine resolvability of radar targets that are separated by time and frequency lags using a given waveform. The Woodward ambiguity function is defined as [6] [17] [24]

$$\chi(\tau, \nu) \triangleq \int_{-\infty}^{\infty} x(t + \frac{\tau}{2})x^*(t - \frac{\tau}{2})e^{-j2\pi\nu t} dt \quad (4.3)$$

$$= \int_{-\infty}^{\infty} \int_{-\infty}^{\infty} W_x(t, f)e^{-j2\pi(\nu t - \tau f)} dt df \quad (4.4)$$

which is the two-dimensional Fourier transform of the Wigner distribution. It can also be defined as the projection of the received signal onto a basis signal that has been time and frequency shifted

$$\chi(\tau, \nu) \triangleq \int_{-\infty}^{\infty} x(t)x^*(t - \tau)e^{-j2\pi\nu t} dt. \quad (4.5)$$

If the Doppler shift ν is set to zero, the cut along the ambiguity function is

$$\chi(\tau, 0) = \int_{-\infty}^{\infty} x(t)x^*(t - \tau)dt, \quad (4.6)$$

which is the autocorrelation function (or the matched filter) of the signal. The squared magnitude of the AF is termed the Ambiguity surface (AS), which forms a maximum likelihood estimator for time delay τ and Doppler ν in radar applications:

$$(\hat{\tau}, \hat{\nu})_{ML} = \arg \max_{\tau, \nu} |\chi(\tau, \nu)|^2. \quad (4.7)$$

Variances of the estimates are traditionally given by the -3dB widths of the peak of the AS [17] [25].

4.2 Arrival Time Estimation

Before estimates of frequency parameters at the temporal center of each pulse can be obtained, pulse arrival times must first be found in order to define the temporal region in which a pulse exists. Determining the pulse arrival time is complicated by noise. In fact, the SNR can be so low that a pulse location cannot be identified in noise, even by envelope detection. One possible way to reduce the effects of noise in the estimate of arrival time is to dechirp the signal using the nominal chirp rate μ and an estimate of the center frequency f_0 . The result is filtered to remove noise outside the signal band, and then rechirped to obtain a signal with higher SNR. Although this technique has the potential to remove some noise from the signal (depending on the signal bandwidth), an estimate of the center frequency is needed to correctly dechirp the signal. If the estimate is incorrect, the filtering process can corrupt the signal instead of removing noise. An alternative to dechirping is envelope detection. This can be used to obtain a rough estimate of arrival time.

Noise in the signal makes the problem of locating pulses nontrivial: simply defining the pulse to start wherever the signal begins to have nonzero amplitude is not possible. Thus, the edge of the noisy pulse must be defined in some other way. Since there is no precise definition of the pulse boundary in the time or frequency domain, we must pick a definition to be consistent.

We define the leading edge and trailing edge of the pulse as the boundaries of a window of nominal pulse width over which the integrated signal power is maximized. Arrival time is defined as the center of this window. A disadvantage of this definition is that the SNR can get so low that the pulse locations become irresolvable by using a metric of signal power.

First, the highest-SNR pulse within the captured data stream may be found by envelope detection, where the signal power is integrated along a sliding window of nominal pulse. The highest apex (Fig. 4.2) in the output reveals the sample corresponding to the trailing edge of the pulse. This technique was suggested by Anderson [2]. Although easy to implement, this method requires *a priori* knowledge of the pulse length, which may vary slightly from its assumed value. However, the length may be estimated by determining boundaries of high-SNR pulses relatively near the pulse under consideration. Obviously,

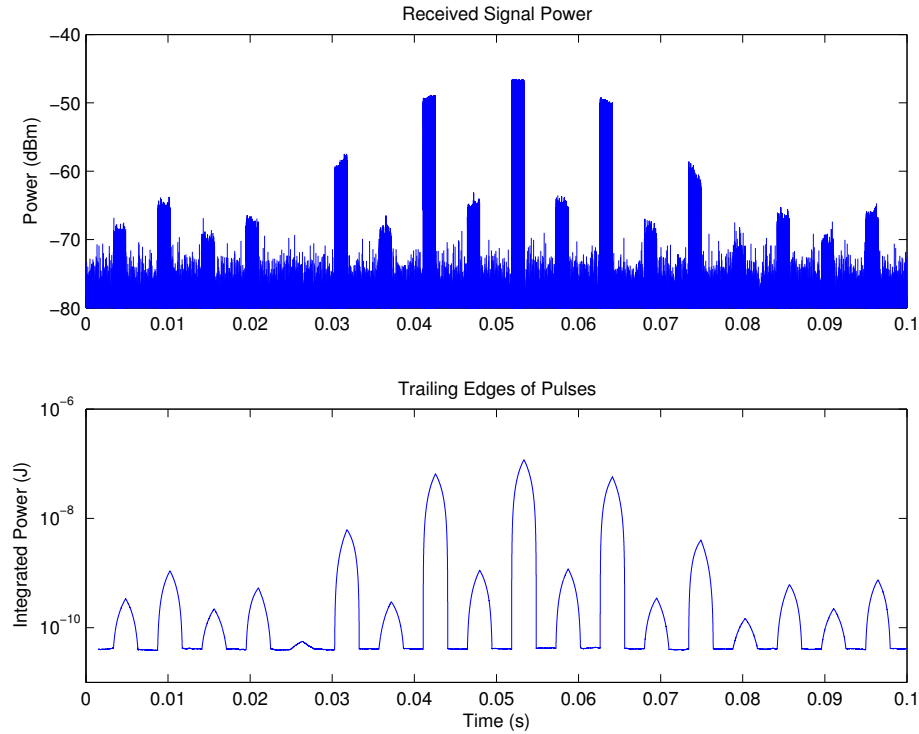


Figure 4.2: Trailing edges of SeaWinds pulses obtained by using an “integrate and dump” incoherent matched filter. The power of the received signal (top) is summed over a sliding window of nominal pulse width. The bottom plot shows the output of the incoherent matched filter, indicating estimated trailing edges.

this can lead to inaccurate estimates of the locations of the leading and trailing edges of the pulse.

A very efficient algorithm for this method may be constructed as follows. Only one initial sum of the first N power samples is needed. As the window of summation is shifted across the data sequence, only one addition (of the next power sample at the trailing edge of the wind) and one subtraction (of the power sample before the leading edge of the window) is needed to compute the total signal power over the sliding window.

Although envelope detection may be used under high-SNR conditions, the performance of this technique to estimate arrival times dramatically deteriorates below 0 dB (see Fig. 4.3). When this technique fails, the arrival times of low-SNR pulses can be estimated by determining the temporal locations of high-SNR pulses in a SeaWinds sweep and then inferring the locations of the low-SNR pulses between sweeps using an estimated PRI. This

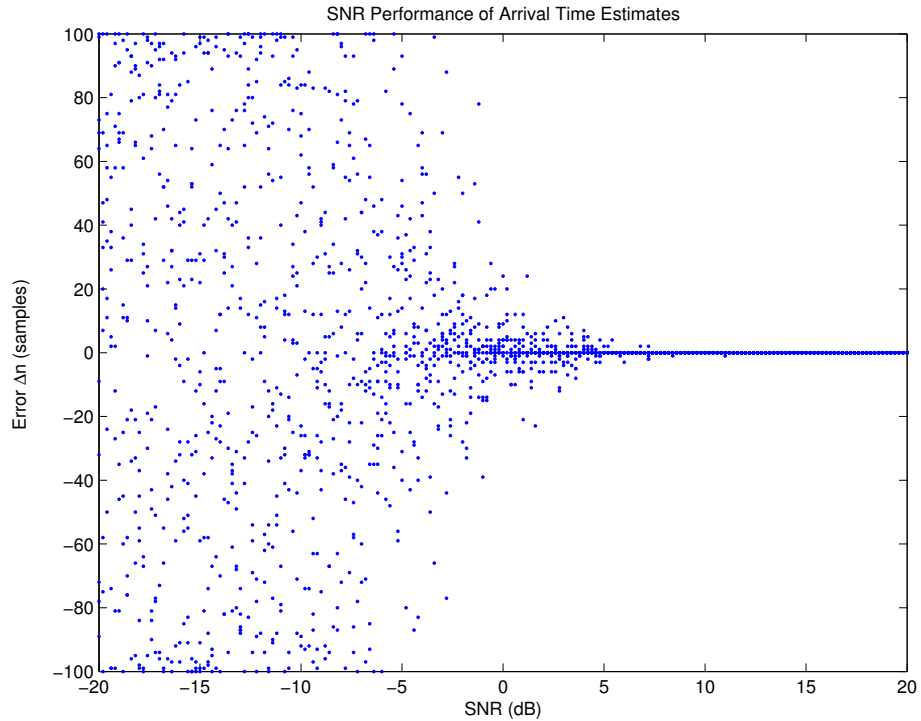


Figure 4.3: Monte Carlo simulation of arrival time estimation by envelope detection. The trailing edges of linear FM pulses are estimated using an “integrate and dump” filter of length $N = 7755$. SNR performance is evaluated from -20 to 20 dB using 10 realizations of white Gaussian noise per SNR increment. The majority of errors occur below 5 dB. Below 0 dB, the method completely fails, leading to sporadic and unreliable arrival time estimates.

assumes the actual PRI deviates only slightly from the approximated PRI due to the change in distance between the CGS and SeaWinds during a flyby. One shortfall of this method is that it estimates the locations of a series of pulses instead of individual ones, assuming individual pulses are perfectly periodic according to the estimated PRI. However, this is the best we can do at low SNR.

4.3 Frequency Estimation

Once the pulse is located and its temporal boundaries determined, the chirp rate and center frequency can be estimated. The parameter of interest is the center frequency since it readily reveals Doppler. This is accomplished by three methods: DFT integration, quadratic regression on signal phase, and a dechirping matched filter bank.

4.3.1 Estimation of Center Frequency by DFT

The simplest estimation method uses the bandwidth of the DFT to infer center frequency within 700 Hz. Once the DFT is obtained, the maximum frequency within a linear FM pulse may be calculated by integrating the DFT magnitude along a sliding frequency interval whose width is the nominal 375-kHz bandwidth. The location of the resulting peak (Fig. 4.4) reveals the trailing edge of the pulse spectrum, corresponding to the maximum frequency of the pulse. This maximum frequency is an estimate of the initial frequency, from which the center frequency can be deduced. One disadvantage of this technique is that its performance is highly dependent on the SNR in the frequency domain since it does not model the signal parametrically. Additionally, its resolution is determined by the density of frequency bins in the DFT (about 700 Hz for SeaWinds pulses). Fig. 4.4 shows the performance of the estimator degrades significantly below 0 dB. Anderson performed this method and then used resolution enhancement techniques in an attempt to increase the accuracy of the estimates [2].

4.3.2 Quadratic Regression on Unwrapped Signal Phase

Another frequency estimation technique involves modeling the signal phase after it has been unwrapped. Phase unwrapping is necessary to recover the signal phase from the wrapped phase that is inherent in discrete-time sampling [26]. The wrapped phase of the analytic chirp signal $x[n]$ may be obtained by taking the arctangent between the real and imaginary parts

$$\angle x[n] = \phi[n] = \arctan \frac{\Im\{x[n]\}}{\Re\{x[n]\}} \quad (4.8)$$

where the range of the multivalued inverse tangent is from $(-\pi, \pi]$. Unwrapping the phase is accomplished by adding $\pm 2\pi$ when the absolute differences between sequential phase values are greater than π radians. As a result, phase unwrapping is prone to offset errors of $\pm 2\pi$ radians which can propagate through the unwrapping process. This is easy to understand in terms of a phasor in a noise cloud. When the noise variance allows the noise cloud to encompass the origin, the phasor can change direction erratically [26]; however, this phase change cannot be distinguished from branch cuts in the complex plane, resulting

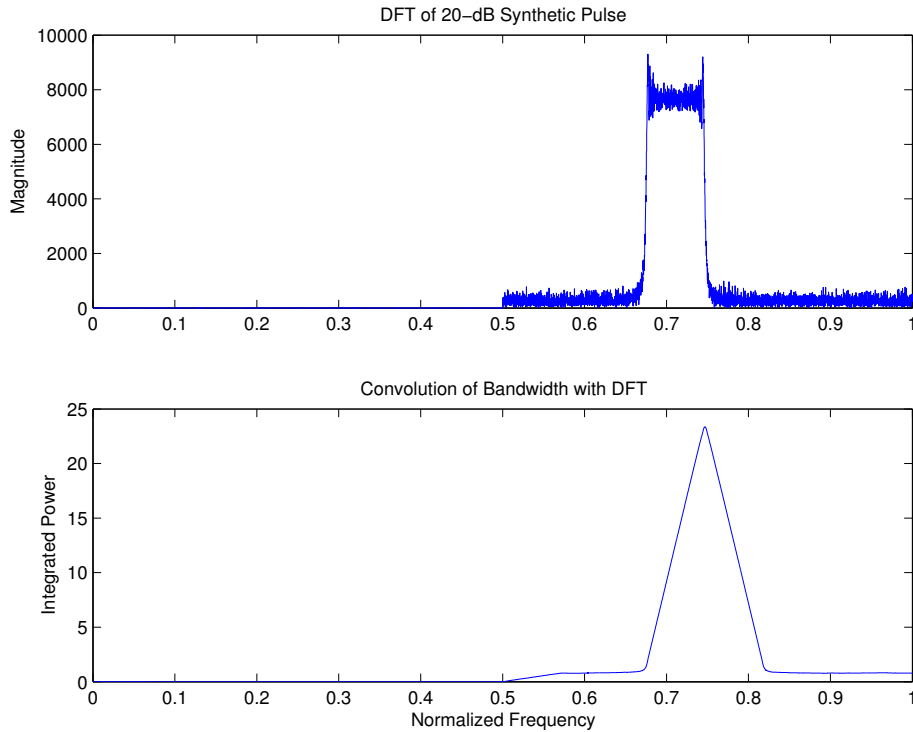


Figure 4.4: DFT method of estimating pulse center frequency f_0 . The DFT magnitude of the analytic signal is convolved with a boxcar of the nominal pulse bandwidth (375 kHz). This implements an “integrate and dump” filter on the magnitude of the signal spectrum, summing the spectrum magnitude over a sliding window. The center frequency is deduced by computing the maximum frequency at the trailing edge of the band and subtracting half the pulse bandwidth (187.5 kHz).

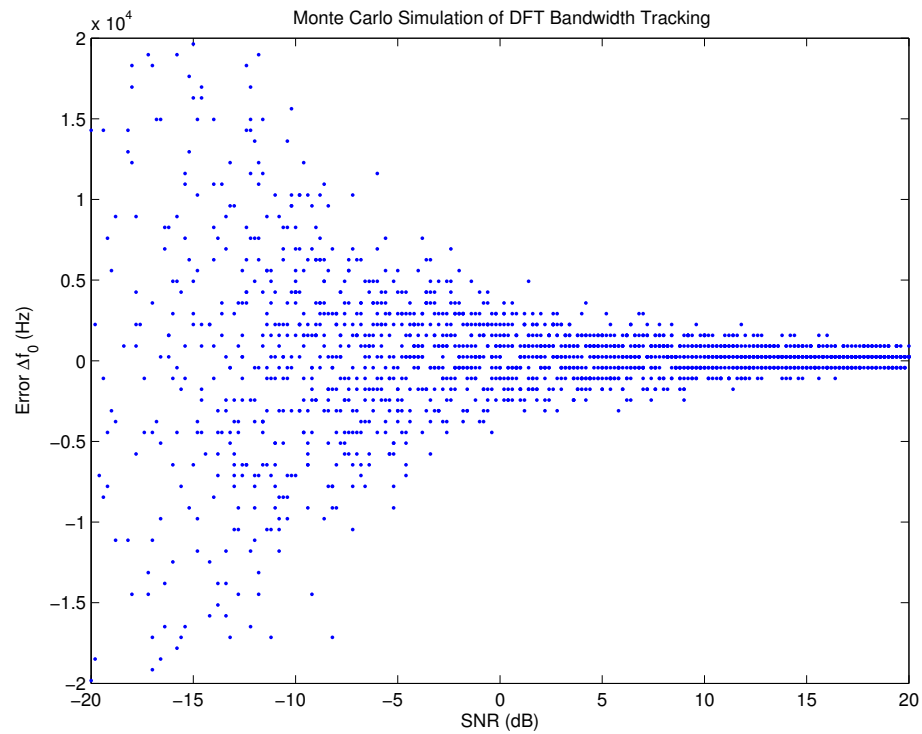


Figure 4.5: Monte Carlo simulation of center frequency estimation using the DFT method. The limited resolution of the DFT method (approximately 700 Hz) is noted by the equally-spaced gaps between the estimates along the frequency axis. This is caused by the DFT, which inherently transforms a discrete signal into discrete frequencies. The method is accurate to within ± 1 kHz at 20 dB SNR, with large error variance below 0 dB.

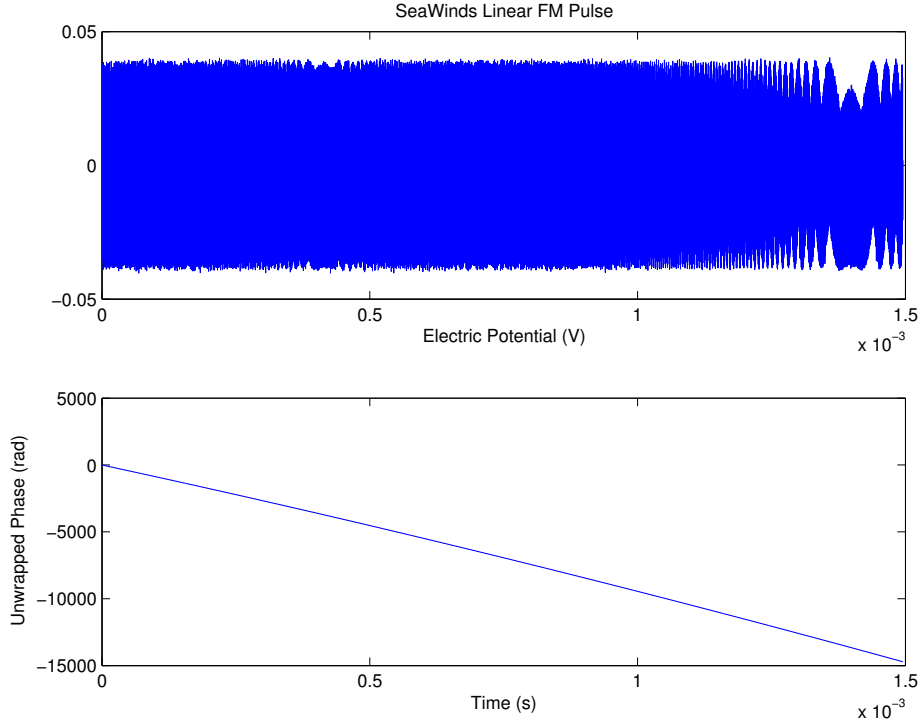


Figure 4.6: Unwrapped phase of a high-SNR SeaWinds pulse. The top plot shows the linear FM pulse as a function of time; the bottom plot reveals the unwrapped phase obtained from the modified analytic signal. The unwrapped phase of the waveform has negative slope and is quadratic, consistent with results expected for a linear FM downchirp.

in a $\pm 2\pi$ error in phase. As such, an SNR above 8 dB [27] and sufficiently dense sampling are desired to accurately unwrap the phase of the signal. The unwrapped phase of a linear FM waveform is quadratic corresponding to linear instantaneous frequency (Fig. 4.6). Once the unwrapped phase has been obtained, it may be modeled as a polynomial, from which the signal parameters may be extracted. Under high-SNR conditions, three phase parameters of a linear FM pulse may be estimated by applying a least-squares approximation to the unwrapped signal phase. This is possible by converting the additive noise $\eta[n]$ in the received waveform into an additive phase noise $w[n]$ [27] [28] such that $\phi(t) = 2\pi \left(\frac{\mu}{2}t^2 + f_0t \right) + \phi_0 + w(t)$.

Applying quadratic regression reveals the chirp rate μ (Hz/s), center frequency f_0 (Hz), and phase offset ϕ_0 (rad). To apply regression to the quadratic phase, we model the

discrete phase as

$$\phi_n \approx \phi_0 + 2\pi f_0 t_n + \pi \mu t_n^2, \quad -\frac{\tau}{2} \leq t_n \leq \frac{\tau}{2}, \quad (4.9)$$

where t_n is the time at sample n , and create a matrix of N rows, corresponding to the number of samples:

$$\begin{bmatrix} \phi_0 \\ \phi_1 \\ \vdots \\ \phi_{N-1} \end{bmatrix} = \begin{bmatrix} \phi_0 + 2\pi f_0 t_0 + \pi \mu t_0^2 \\ \phi_0 + 2\pi f_0 t_1 + \pi \mu t_1^2 \\ \vdots \\ \phi_0 + 2\pi f_0 t_{N-1} + \pi \mu t_{N-1}^2 \end{bmatrix} + \begin{bmatrix} e_0 \\ e_1 \\ \vdots \\ e_{N-1} \end{bmatrix}. \quad (4.10)$$

If we let

$$\boldsymbol{\phi} = \begin{bmatrix} \phi_0 \\ \phi_1 \\ \vdots \\ \phi_{N-1} \end{bmatrix}, \quad A = \begin{bmatrix} 1 & 2\pi t_0 & \pi t_0^2 \\ 1 & 2\pi t_1 & \pi t_1^2 \\ \vdots & \vdots & \vdots \\ 1 & 2\pi t_{N-1} & \pi t_{N-1}^2 \end{bmatrix}, \quad \mathbf{c} = \begin{bmatrix} \phi_0 \\ f_0 \\ \mu \end{bmatrix}, \quad \mathbf{e} = \begin{bmatrix} e_0 \\ e_1 \\ \vdots \\ e_{N-1} \end{bmatrix}, \quad (4.11)$$

Eq. 4.10 becomes

$$\boldsymbol{\phi} = A\mathbf{c} + \mathbf{e}. \quad (4.12)$$

To obtain the best least-squares estimate of the parameter vector \mathbf{c} (which lies in the range space of A), we project $\boldsymbol{\phi}$ onto the range of A , such that $\mathbf{c} = (A^H A)^{-1} A^H \boldsymbol{\phi}$, and obtain the phase estimate $\hat{\boldsymbol{\phi}} = A\mathbf{c}$.

An equivalent technique is to apply a least-squares approximation to the zero-crossing times t_k of the signal, where the subscript n has been replaced with k to indicate zero-crossings k instead of samples n . Notice that the phase vector $\boldsymbol{\phi}$ is easily found by setting the phase argument equal to odd multiples of $\frac{\pi}{2}$, $\phi_k = (2k + 1)\frac{\pi}{2}$, which correspond to the zero-crossings of a cosine. First, however, the zero-crossing times t_k must be obtained. A zero-crossing must occur somewhere between coupled samples that are opposite in sign. Using the point-slope equation

$$x_{n+1} - x_n = m(t_{n+1} - t_n), \quad (4.13)$$

where x_n is the real signal, m is the linearly interpolated slope, and t_n is the sample time, we calculate the slope m between samples n and $n + 1$ and use the slope-intercept equation

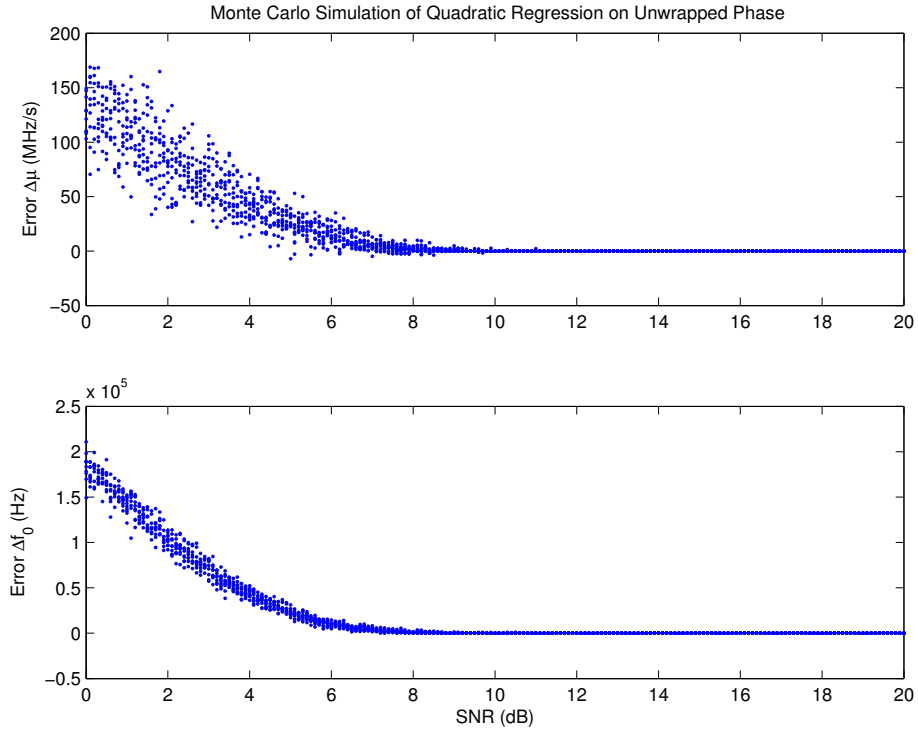


Figure 4.7: Monte Carlo simulation of chirp rate and center frequency estimates using quadratic regression on unwrapped phase. The top plot shows error in chirp rate estimates as a function of SNR; likewise, the bottom plot indicates error in center frequency estimates. The synthetic linear FM waveforms are generated using the nominal SeaWinds parameters for chirp rate ($\mu = -250.73$ MHz/s) and center frequency ($f_0 = 3.875$ MHz) over 10 realizations at each SNR level, simulated by adding white Gaussian noise. Although both estimates start to converge to their true values above 8 dB SNR (which is consistent with results obtained by Djurić and Kay [27]), the estimates only completely converge above 11 dB due to errors in phase unwrapping. Estimates unaffected by unwrapping errors are accurate to within ± 5 kHz. This is a significant improvement over the DFT method; however, since it is only usable above 8 dB SNR (which is frequently above the SNR of most SeaWinds pulses), it is not well suited to use in estimating SeaWinds phase coefficients.

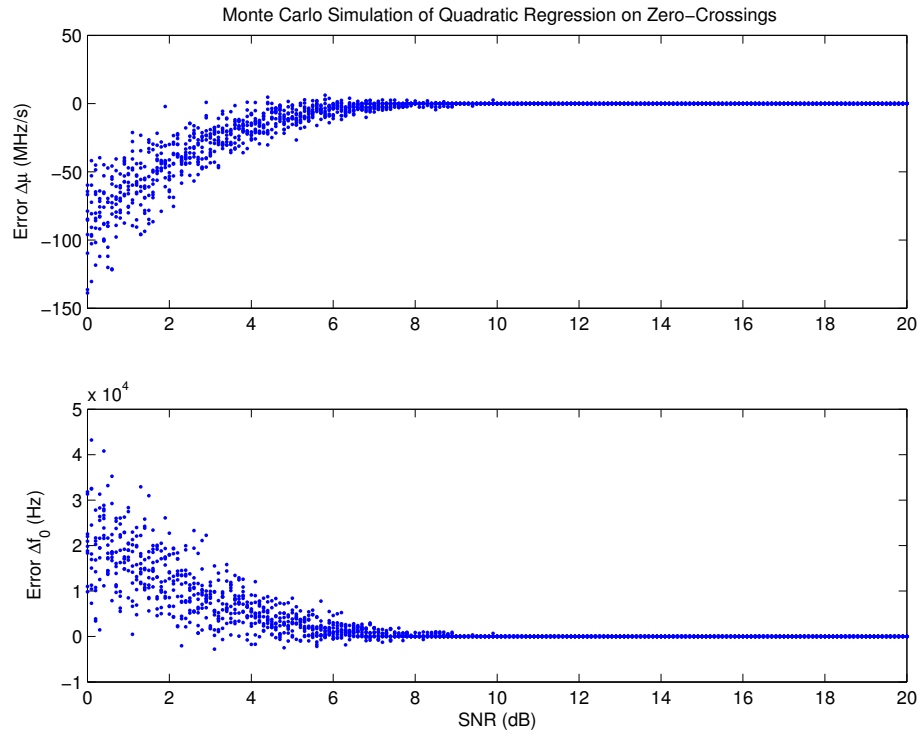


Figure 4.8: Monte Carlo simulation of quadratic regression on zero crossings. The synthetic waveforms used in this simulation are identical to those used in the simulation of Fig. 4.7, as is the layout of the plots. Since the zero-crossings are computed from the real signal, the estimates correspond to the first half of the signal spectrum (which is the wrong spectrum due to undersampling) such that $\mu = 250.73$ MHz/s and $f_0 = 1.3125$ MHz. These differences are taken into account in the above plots. Error variance depends on the existence of zero-crossing errors. If zero-crossing errors do not occur, the method estimates the center frequency to within ± 5 kHz. The estimates begin to converge to the true values above 7 dB, doing so completely above 10.5 dB.

$m(t_k - t_n) + x_n = 0$ to obtain the linearly interpolated zero-crossing time $t_k = t_n - x_n/m$. Linear interpolation may be justified by observing the linear portion of the cosine function near the zero-crossings of the waveform. Interpolation accuracy may be increased by upsampling the waveform to a higher sampling rate. This allows the estimation of zero crossings to be more accurate by linearly interpolating between samples that are closer to the linear portion of the sinusoidal waveform.

Recall that the cosine function contains zero-crossings at odd multiples of $\frac{\pi}{2}$. It is imperative to distinguish between the zero-crossing at $\frac{\pi}{2}$ and that at $\frac{3}{2}\pi$, in order to avoid phase errors of π radians. This distinction is easily made by noticing that the cosine function at the $\frac{\pi}{2}$ zero-crossing has a negative slope while at $\frac{3}{2}\pi$ it has a positive slope.

Regression on signal phase is difficult to perform at low SNR. Monte Carlo simulations of phase regression using phase unwrapping (Fig. 4.7) and zero-crossings (Fig. 4.8) reveal very demanding SNR requirements for reliable estimates. This limits their usefulness. Although the method is more complex and computationally intensive than the DFT method, its results are much more accurate for SNR above 8 dB. Additionally, the chirp rate and phase coefficients are jointly estimated with the center frequency, which creates an estimate of the entire signal phase.

4.3.3 Dechirping Matched Filter Bank

The maximum likelihood estimator of linear FM signal parameters $\theta = [\mu f_0]^T$ in complex white Gaussian noise (CWGN) $\eta[n]$ with variance σ_η^2 consists of dechirping the signal over a range of these parameters. The probability density function (pdf) of the random variable $X[n]$ is

$$f_X(x[n]; \theta) = \frac{1}{\sqrt{2\pi\sigma}} \exp \frac{-(x[n] - s[n; \theta])^2}{2\sigma^2}. \quad (4.14)$$

Since the random noise sequence is independent and identically distributed, the covariance matrix $C = \sigma^2 I$ is diagonal, and the likelihood function becomes the multivariate Gaussian pdf

$$f_{\mathbf{X}}(\mathbf{x}; \theta) = \prod_{n=0}^{N-1} f_X(x[n]; \theta) \quad (4.15)$$

$$= \frac{1}{(2\pi)^{\frac{N}{2}} |C|^{\frac{1}{2}}} \exp \left[-\frac{1}{2} (\mathbf{x} - \mathbf{s})^H C^{-1} (\mathbf{x} - \mathbf{s}) \right] \quad (4.16)$$

$$= \frac{1}{(2\pi\sigma^2)^{\frac{N}{2}}} \exp \left[-\frac{1}{2\sigma^2} \sum_{n=0}^{N-1} |x[n] - s[n]|^2 \right]. \quad (4.17)$$

To estimate the parameters $\boldsymbol{\theta}$, the log-likelihood function $\Lambda(\boldsymbol{\theta}, \mathbf{x}) = \log f_X(\mathbf{x}; \boldsymbol{\theta})$ is maximized by minimizing $(\mathbf{x} - \mathbf{s})^H (\mathbf{x} - \mathbf{s})$. It can be shown that the ML estimate of $\boldsymbol{\theta}$ is [29] [30]

$$\hat{\boldsymbol{\theta}} = \arg \max_{\boldsymbol{\theta}} \left| \sum_{n=0}^{N-1} x[n] e^{-j2\pi(f_0 n + \frac{\mu}{2} n^2)} \right|^2, \quad (4.18)$$

which results in a coarse search over the parameters for the best correlated match between the received signal and a linear FM pulse [29] (See Fig. 4.9).

The Cramer-Rao Bound (CRB) for each parameter is inversely proportional to SNR (σ_η^2/A^2) and depends on the initial sample n_0 . When the sequences are centered around $n = 0$, such that $n_0 = -(N - 1)/2$, the CRBs are minimized and given by [27]

$$\begin{aligned} \sigma_{\hat{\mu}}^2 &\geq \frac{\sigma_\eta^2}{A^2} \frac{1}{\pi^2} \frac{90}{N(N^2-1)(N^2-4)} \\ \sigma_{\hat{f}}^2 &\geq \frac{\sigma_\eta^2}{A^2} \frac{1}{\pi^2} \frac{3}{2N(N^2-1)}. \end{aligned} \quad (4.19)$$

At sufficient SNR, the ML estimator meets these bounds asymptotically [29] (See Fig. 4.10). By comparing Monte Carlo simulations, the dechirping method outperforms the DFT method at all SNR levels and performs better than the phase regression method for SNR below 8 dB.

Although error variance starts to increase significantly below -12 dB, the estimate error is still within ± 50 Hz at -12 dB. The price of this performance is the heavy computational intensity of the algorithm, where a coarse grid must be computed and searched.

The Radon Transform of the WD (Sec. 3.7) has been shown to be equivalent to dechirping [19] [21]

$$g(r, \theta) = \int W_x(t, f_0 + \mu t) dt = \left| \frac{1}{\sqrt{2\pi}} \int x(t) e^{-j2\pi(f_0 t + \frac{\mu}{2} t^2)} dt \right|^2 \Bigg|_{\substack{\mu = -\cot(\theta)/2\pi \\ f_0 = r/2\pi \sin(\theta)}}. \quad (4.20)$$

In discrete time, we have

$$\sum_n W_x^e(n, f_0 + \mu n) = \left| \frac{1}{\sqrt{N}} \sum_{n=0}^{N-1} x[n] e^{-j2\pi(f_0 n + \frac{\mu}{2} n^2)} \right|^2 \quad (4.21)$$

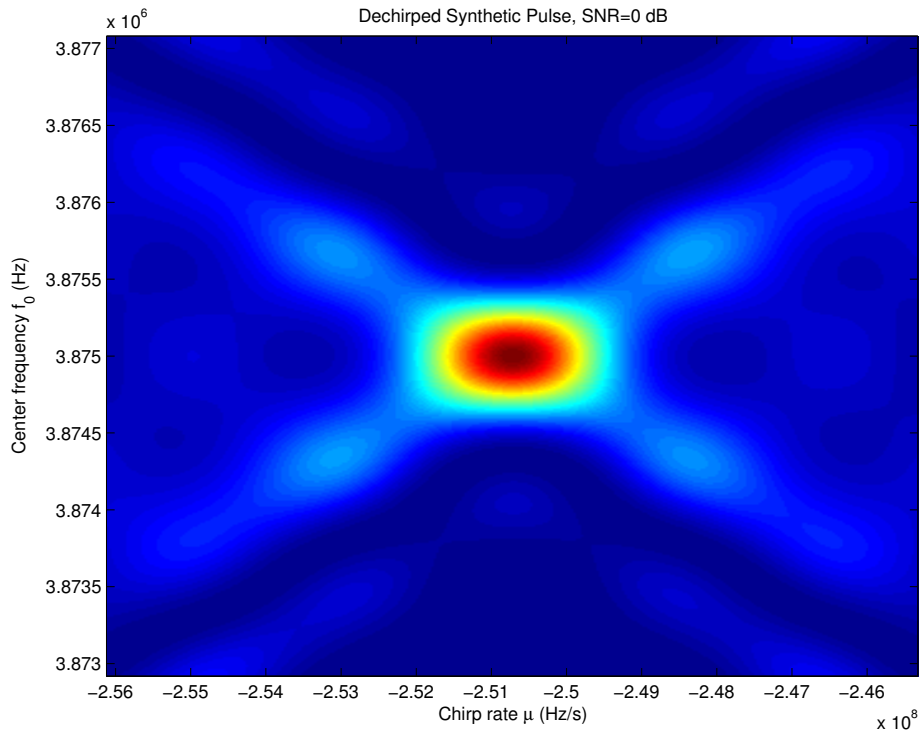


Figure 4.9: Output of dechirping matched filter bank parameterized by chirp rate μ and center frequency f_0 . A 0-dB synthetic linear FM pulse is generated using the nominal SeaWinds parameters $\mu = -250.73$ MHz/s and $f_0 = 3.875$ MHz. Eq. 4.18 is implemented by projecting the signal onto each waveform in the filter bank. A coarse search over the parameter grid finds the maximum correlation between the signal and one of the functions in the filter bank. The parameters of this matching function are then accepted as the parameter estimates. In this plot, the maximum correlation occurs at the center of the main lobe indicated in dark red. This main lobe contracts as the signal length is increased, allowing more accurate estimates of longer signals.

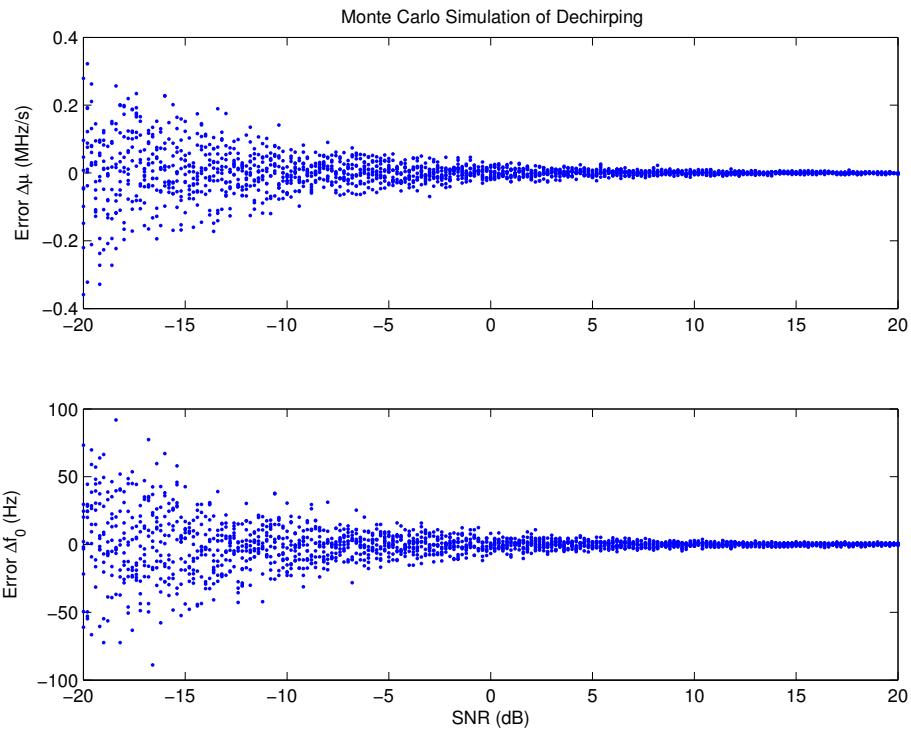


Figure 4.10: Monte Carlo simulation of chirp rate and frequency estimates using the dechirping matched filter bank method. The top plot shows error in chirp rate estimates as a function of SNR; the bottom plot indicates error in center frequency estimates. At each SNR level, 10 realizations of synthetic linear FM waveforms were generated by adding white Gaussian noise to pulses with nominal SeaWinds parameters for chirp rate ($\mu = -250.73$ MHz/s) and center frequency ($f_0 = 3.875$ MHz). The SNR performance is exceptional. At 20 dB, the estimates are accurate to within ± 2 Hz; at -20 dB, the estimates are still within ± 80 Hz. The performance of the estimator deteriorates gradually with SNR, experiencing no threshold effect like that of the DFT or phase regression methods.

where W_x^e is the Extended Discrete-Time WD defined as

$$W_x^e(n, f) = \sum_{k: n \pm \frac{k}{2} \in \mathbb{Z}} x[n + \frac{k}{2}]x^*[n - \frac{k}{2}]e^{-j2\pi fk}, n \in \frac{\mathbb{Z}}{2}. \quad (4.22)$$

Hence, integrating all lines in the time-frequency plane is statistically equivalent to dechirping the signal over a matched filter bank. Although dechirping may be more efficient than computing the WD and then integrating along all lines in the TF plane, it still poses a heavy computational burden.

4.4 Summary

The optimal estimation of chirp rate and center frequency is performed by projecting the signal onto a matched filter bank and obtaining the parameter estimates that yield maximum correlation with the received signal. The disadvantage of this method is its computational intensity. For signals that meet a high SNR threshold, quadratic regression on signal phase is an acceptable suboptimal method. The DFT method is the least computationally complex, and also the least accurate. It should only be employed as a rough estimate when accuracy is not an issue.

These methods are all based on the assumption that the pulse boundaries are accurately known. At low SNR, pulse arrival times must simply be inferred from surrounding high-SNR pulses and an estimated PRI. If this assumption is inaccurate, the frequency estimates of all our methods yield inaccurate results because the estimated temporal centers of the pulses are in error. The application of these methods to real SeaWinds data is shown in Chapter 5.

Chapter 5

Results

This chapter applies the frequency estimation methods of Chapter 4 to real SeaWinds data captures. Before the estimation methods can be performed, pulse arrival times must first be estimated. Doppler compensation and Doppler shift may then be resolved through a model that separates the two parameters. The performance of the Doppler model using each estimation method is analyzed. Limitations in sample rate and arrival time estimation impede further performance enhancement.

5.1 Sample Rate Limitations

Since many pulses in captured SeaWinds transmissions have low SNR, high-SNR pulses that occur during sweeps are located first using envelope detection. From these reference pulses, the locations of pulses with low SNR can be deduced using an estimated PRI that is updated from sweep to sweep. Although the accuracy of pulse centers obtained from this technique is difficult to verify, it is probably the best we can do to estimate the pulse locations. Resolution of these arrival time estimates is limited by the sample rate of the CGS. This, in turn, limits the resolution of center frequency estimates. At a sample rate of 5.1875 MSPS, the center frequency estimated by an ideal estimator changes by approximately 48 Hz for every sample that the estimated pulse center deviates from the actual pulse center. This can be shown by dividing the nominal pulse bandwidth by the pulse width (in samples). Although this has little effect on the DFT method, the dechirping method is hampered by this limitation. As a result, its performance does not achieve its potential; to do so would require a higher sample rate and more accurate methods to estimate pulse arrival times. Nevertheless, dechirping still produces more accurate results than other techniques.

5.2 Initial Estimates

Recall that the SeaWinds Doppler compensation algorithm is designed to cancel the two-way Doppler effect in the received RCS backscatter by varying the Doppler compensation sinusoidally as a function of the 18-rpm antenna rotation. Hence, the CGS observes the sum of the two-way commanded Doppler compensation and the one-way Doppler shift caused by the QuikSCAT satellite approaching (or receding) from the CGS. This causes a sinusoidal oscillation and a bias in the observed center frequencies of consecutive pulses (Fig. 5.1). After the center frequency estimates, the next task is to estimate the Doppler compensation and Doppler shift. In order to estimate the Doppler shift and the amplitude of the Doppler compensation sinusoid from the sequence of received center frequencies, a model must be imposed on the data.

5.3 Separation of Doppler Compensation and Doppler Shift

Since the relative velocity of the satellite with respect to the CGS compresses received pulses along the time axis (by α), Doppler shift is observed in data received from the SeaWinds instrument. The center frequency of each SeaWinds pulse received by the CGS is dependent on the phase of the Doppler compensation algorithm and the time compression factor α . From Eq. 3.7, the center frequency is

$$f_0 = [f_c + \nu_c \cos(\phi_c)]\alpha = f_c + \nu_c \cos(\phi_c) + \nu_d, \quad (5.1)$$

which is the sum of the nominal carrier frequency f_c , Doppler compensation $\nu_c \cos(\phi_c)$, and Doppler shift ν_d . The Doppler shift is then

$$\nu_d = [f_c + \nu_c \cos(\phi_c)](\alpha - 1) \quad (5.2)$$

at pulse center. To resolve estimates of Doppler compensation and Doppler shift, these parameters must be separated from the received center frequency f_0 . To do so, a nonlinear least-squares approximation can be used to fit f_0 to Eq. 5.1, revealing estimates of ν_c and ν_d . First, however, the Doppler shift must be modeled.

An approximation to the Doppler shift for LEO satellites can be parameterized by the minimum zenith angle θ_{min} and the angular velocity of the satellite [31]. θ_{min} is obtained by measuring the angle to the satellite at the zero-Doppler instant, where the satellite

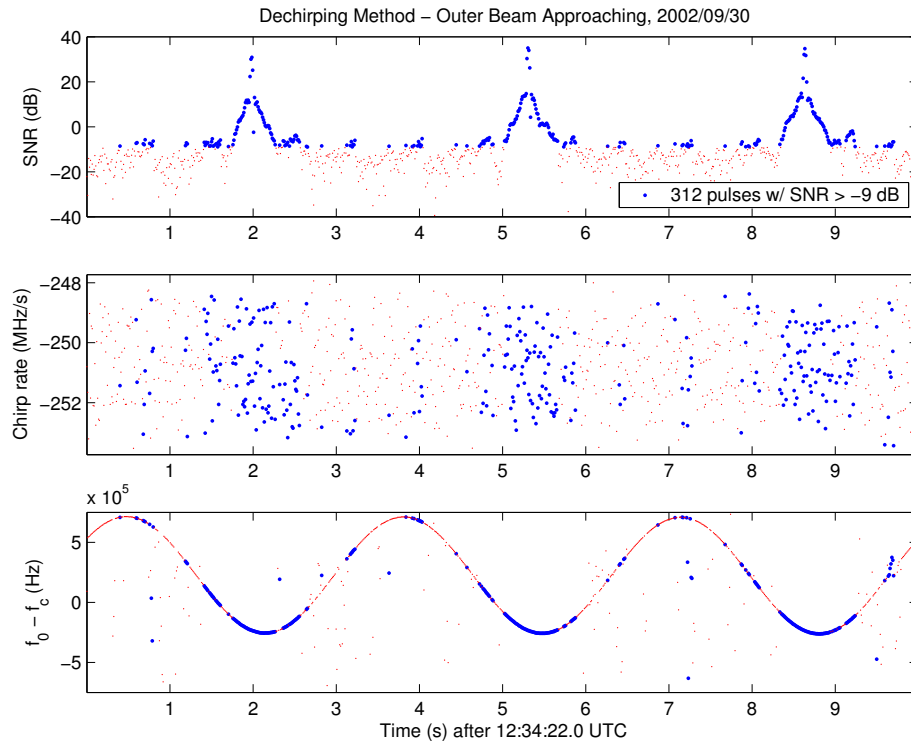


Figure 5.1: Three plots showing SNR (top), chirp rate (middle), and deviation from nominal center frequency (bottom) for each pulse in a capture of 3 SeaWinds sweeps from one pass in September 2002. The SNR is calculated by computing the ratio of average pulse power to average noise power over an interval where no pulses occur. The envelope of the SeaWinds antenna pattern can be seen in the SNR plot. The chirp rate and frequency estimates are obtained using the dechirping method. Estimates of the chirp rate hover around the nominal -250.73 MHz/s. The majority of the pulses above -9 dB yield frequency estimates that track a sinusoid. The sinusoidal oscillation is caused by the commanded Doppler compensation algorithm.

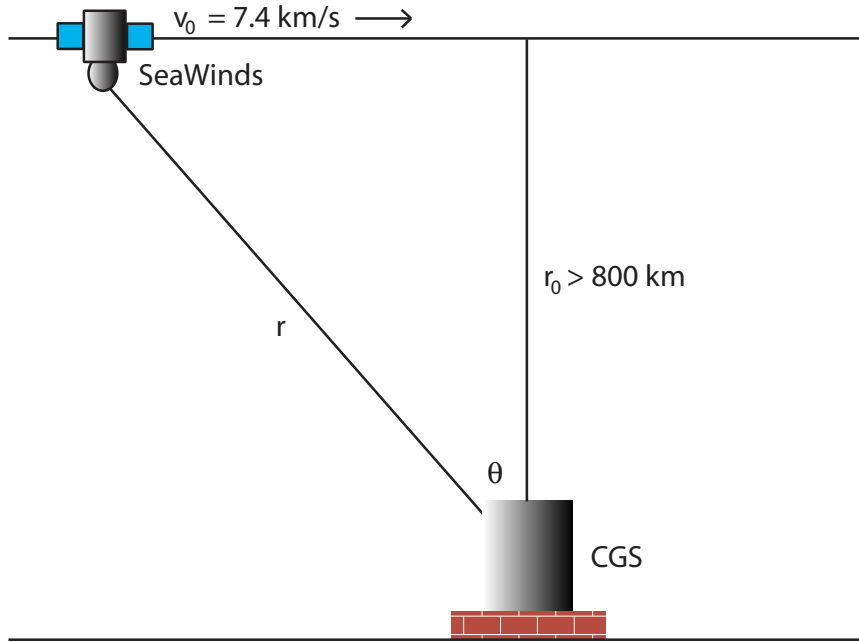


Figure 5.2: Simplified geometry of the SeaWinds scatterometer and the CGS during a flyby. Instead of accounting for the curvature of the satellite orbit, the satellite is assumed to fly a straight path over the CGS. Although this assumption is only approximate, it greatly simplifies modeling the Doppler effect for a small, 10-s interval when the CGS captures SeaWinds transmissions.

is closest in range to the CGS. However, since the main constraint in Eq. 5.1 is ν_c , the equation of ν_d can be simplified due to the short time interval over which the center frequencies are observed. For our purposes of modeling the Doppler shift, a simplified expression of the relative velocity of SeaWinds with respect to the CGS is obtained by assuming a straight trajectory of the QuikSCAT satellite over the CGS during a flyby (Fig. 5.2). This approximation is fairly accurate over this short time interval. The range to the satellite is

$$r(t) = \frac{r_0}{\cos \theta(t)}, \quad (5.3)$$

where $r_0 = r(0)$ is the closest distance that the satellite approaches the CGS. This value is approximately 800 km for flybys directly over the CGS, but usually is more since the satellite usually does not pass directly over it. Knowing $r(t)$, the relative velocity with

respect to the CGS is

$$v = -\frac{dr(t)}{dt} = -\frac{d}{dt} \left[\frac{r_0}{\cos \theta(t)} \right] = -r_0 \tan \theta(t) \sec \theta(t) \frac{d}{dt} \theta(t). \quad (5.4)$$

The Doppler compensation bias $\nu_c \cos(\phi_c)$ has a negligible effect ($\nu_c \ll f_c$) in Eq. 5.2. Therefore, we eliminate the Doppler compensation term and substitute Eq. 5.4, yielding

$$\nu_d \approx f_c(\alpha - 1) = f_c \frac{v}{c} = -\frac{f_c}{c} r_0 \tan \theta(t) \sec \theta(t) \frac{d}{dt} \theta(t). \quad (5.5)$$

Since $\tan \theta(t) = \frac{x(t)}{r_0}$, we have

$$\theta(t) = \arctan \frac{-x(t)}{r_0} \quad (5.6)$$

$$\frac{d}{dt} \theta(t) = \frac{-v_0}{r_0} \frac{1}{1 + \left(\frac{-x(t)}{r_0} \right)^2}. \quad (5.7)$$

Assuming the flat-Earth satellite ground track is $x(t) = v_0(t - t_0)$, where the satellite velocity is $v_0 = 7.4$ km/s and t_0 is the zero-Doppler instant, we obtain a simplified equation to approximate the observed Doppler shift

$$\nu_d \approx -\frac{f_c v_0}{c r_0} \frac{x(t)}{1 + \left(\frac{-x(t)}{r_0} \right)^2} \sec \left[\arctan \left(\frac{-x(t)}{r_0} \right) \right]. \quad (5.8)$$

We are now ready to separate Doppler compensation and Doppler shift from the center frequency f_0 . Substituting Eq. 5.8 into Eq. 5.1, we obtain

$$f_0 = f_c + \nu_c \cos(\phi_c) - \frac{f_c v_0}{c r_0} \frac{x(t)}{1 + \left(\frac{-x(t)}{r_0} \right)^2} \sec \left[\arctan \left(\frac{-x(t)}{r_0} \right) \right]. \quad (5.9)$$

A nonlinear least-squares approximation is then used to fit the sequence of received center frequencies to this model, revealing estimates of Doppler compensation and Doppler shift.

5.4 Comparison of Estimation Methods Used by the Doppler Model

Performance of the Doppler model using three estimation methods is compared using a September 2002 data set. The performance of this model is affected by the accuracy of the center frequencies estimated and the number of pulses included in the nonlinear regression of the model.

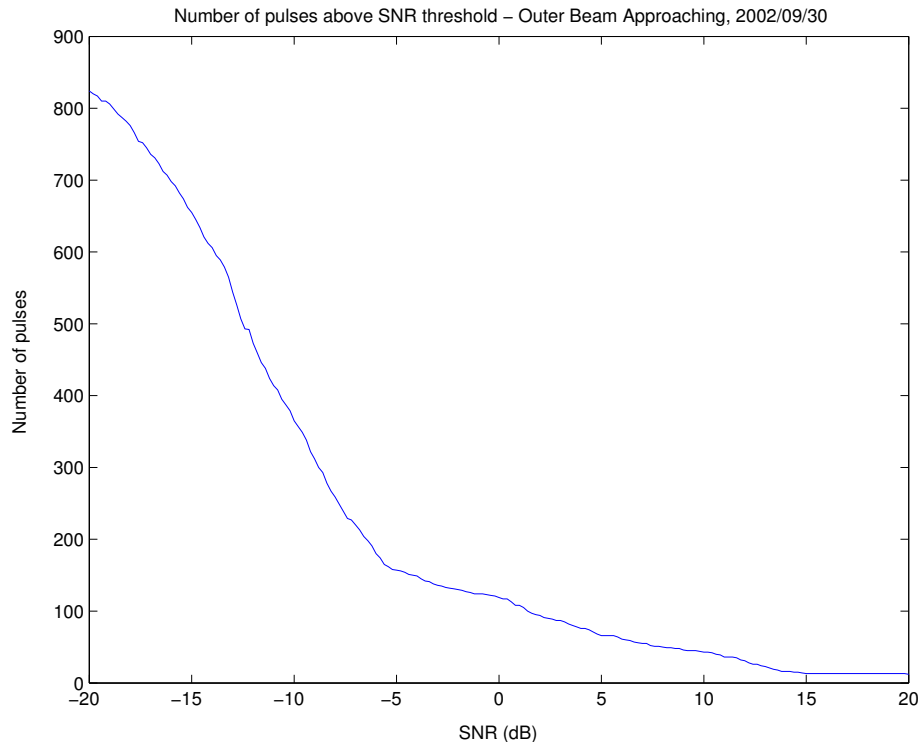


Figure 5.3: Number of pulses in a 10-s capture considered in the Doppler model as a function of SNR threshold. The outer beam of this data set yields only 157 pulses with SNR greater than -5 dB (out of a nominal 925). Since the performance of estimation methods is degraded at low SNR, an SNR threshold is used to select pulses for a model that separates the Doppler compensation and Doppler shift parameters. This threshold is necessary to exclude inaccurate frequency estimates from inclusion in the Doppler estimates.

Since the SeaWinds instrument illuminates the CGS in sweeps, many of the pulses in CGS captures have low SNR. Figure 5.3 shows the number of pulses that the Doppler model considers as a function of the SNR threshold for a sample data set. This shows that the majority of pulses have SNR below -5 dB. In Chapter 4 the accuracy of the DFT is shown to degrade to ± 10 kHz at this SNR. The high SNR requirement of the phase regression method prohibits it from using a large number of pulses for estimation of Doppler parameters. Since the dechirping method has excellent performance at low SNR, incorporation of the dechirping method in the Doppler model is expected to yield less variance in modeling error.

Results of the Doppler model obtained using the DFT method are shown in Fig. 5.4. The DFT method includes 136 pulses using a -3 dB SNR threshold, since below this

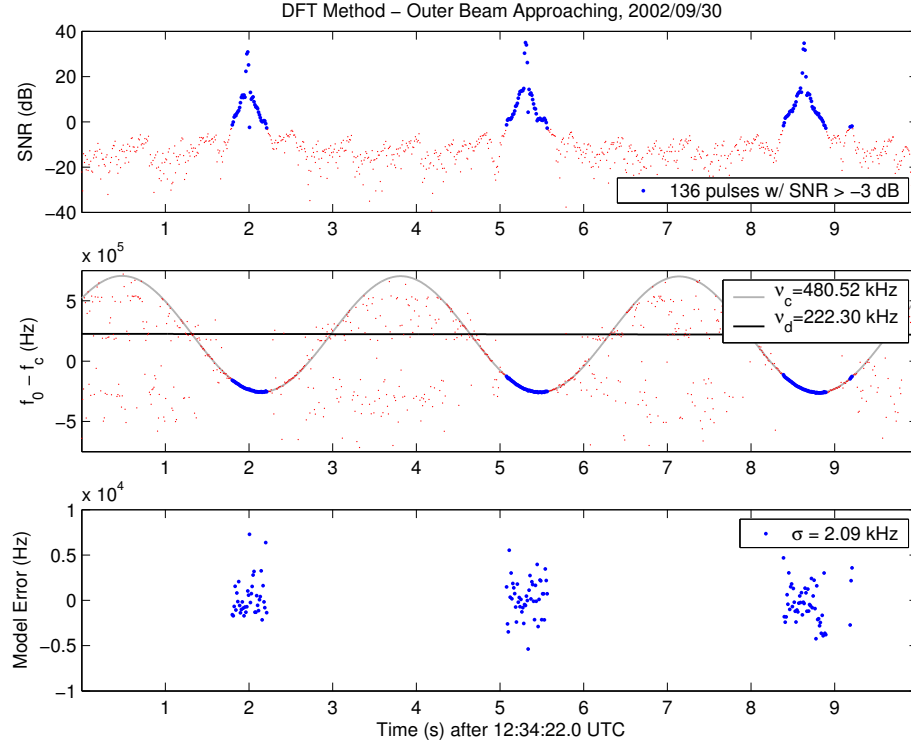


Figure 5.4: Results of performing the DFT method on SeaWinds pulses. The top plot indicates the computed SNR of each pulse. The middle plot shows the deviation of the received center frequency f_0 of each pulse from the nominal center frequency $f_c = 13.402$ GHz. These frequencies are then modeled as described in Sec. 5.3, yielding estimates of maximum Doppler compensation ν_c and Doppler shift ν_d . The bottom plot reveals the deviation of the center frequencies from the fitted model. Since the resolution of the DFT is approximately 700 Hz, the standard deviation of the model error is the highest among the three presented methods. Note that many low-SNR pulses (indicated in red) yield sporadic frequency estimates using the DFT method.

threshold the estimate quality deteriorates. The Doppler model estimates the amplitude of the Doppler compensation sinusoid to be $\nu_c = 480.52$ kHz. This is close to the nominal 480 kHz. The Doppler shift is estimated to be $\nu_d = 222.30$ kHz. A slightly attenuated Doppler is explained by SeaWinds not passing directly over the CGS, decreasing the relative velocity of the satellite. The difference between the frequency estimates and the model is rather high at a standard deviation of 2.09 kHz. This is explained by the low resolution of the DFT method.

The performance of the Doppler model using the phase regression method is shown in Fig. 5.5. Due to the dependence of phase regression on SNR, the Doppler model is

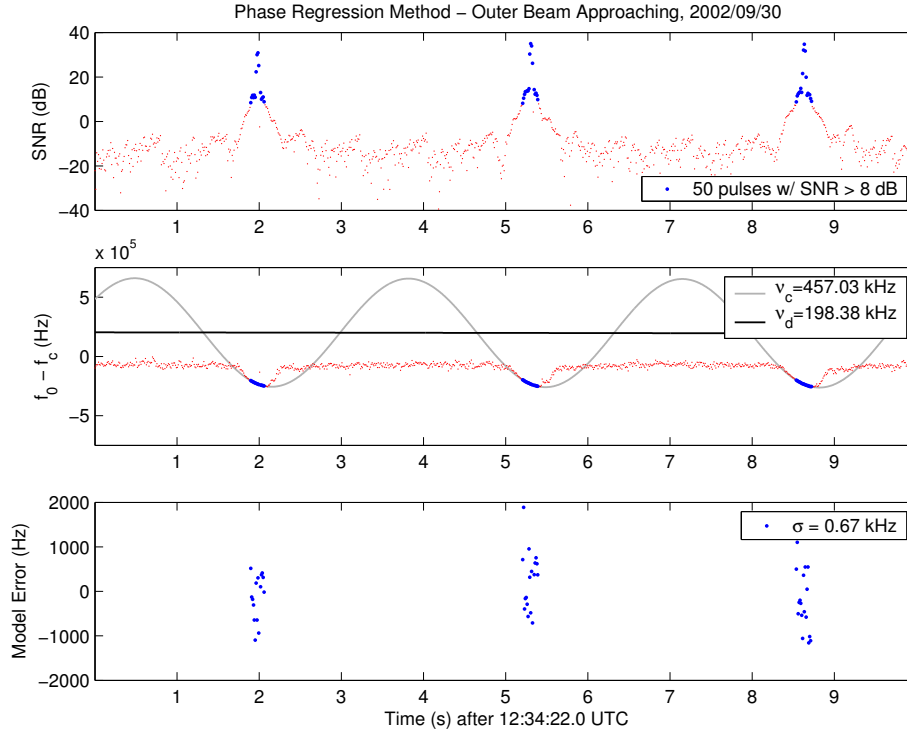


Figure 5.5: Results of performing the phase regression method on SeaWinds pulses. All three plots are in the same format as Fig. 5.4. Since this method does not work below 8 dB, only very few pulses are included in the Doppler model, leading to less reliable estimates of Doppler compensation and Doppler shift. However, the model error has decreased from that given by the DFT method.

restricted to pulses with SNR greater than 8 dB. As such, only 50 pulses are considered. The Doppler model estimates $\nu_c = 457.03$ kHz and $\nu_d = 198.38$ kHz. Even though the standard deviation of the model error is 0.67 kHz, too few pulses are included in the data model to yield an accurate estimate of the Doppler parameters.

Since the dechirping method yields the best performance under low-SNR conditions, more pulses can be included in the Doppler model (Fig. 5.6). The SNR threshold is lowered to -6 dB, incorporating 180 pulses. Lowering the threshold beyond -6 dB results in outlier frequency estimates, severely corrupting the Doppler model. The Doppler model estimates the Doppler compensation $\nu_c = 484.00$ kHz and Doppler shift $\nu_d = 225.86$ kHz, which is very close to estimates obtained by using the DFT method. The standard deviation of the center frequency estimates from the Doppler model (0.99 kHz) is less than half that

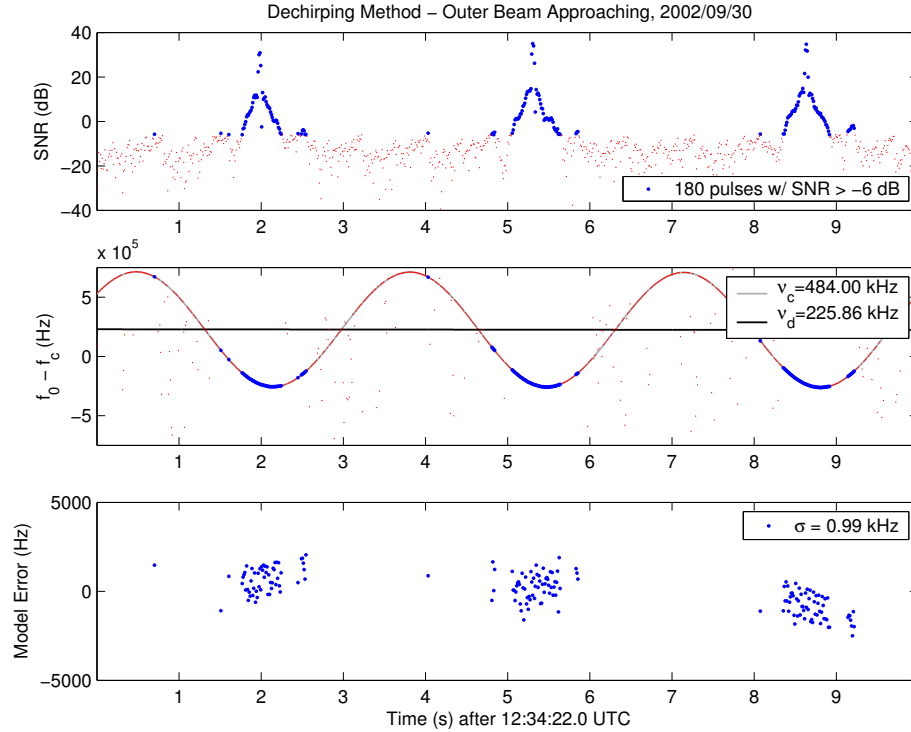


Figure 5.6: Results of performing the dechirping matched filter bank method on SeaWinds pulses. All three plots are in the same format as Fig. 5.4. Since the dechirping method is accurate and has no SNR threshold where estimator performance dramatically deteriorates, pulses at lower SNR are included in the Doppler model. This results in the inclusion of more data points, increasing the accuracy of the model estimates. Even with more data points at lower SNR, model error decreases compared to other methods. These results generally agree with the DFT method but have lower Doppler error.

obtained from the DFT method, even though more points are included than the number included by the DFT method. As expected, the dechirping method outperforms the DFT and phase regression methods. However, its accuracy is affected by precision of arrival time estimates, which are limited by sample rate. This limits the resolution of any frequency estimation method to at least 48 Hz of resolution.

The performance of the Doppler model is better determined by evaluating the estimation methods over a range of SNR. Standard deviation of the center frequency estimates from the Doppler model are shown in Fig. 5.7 for each method. Use of the DFT method in the Doppler model leads to model convergence above -5 dB SNR with standard deviation between 1 and 2 kHz. Use of the model with the phase regression method does not begin

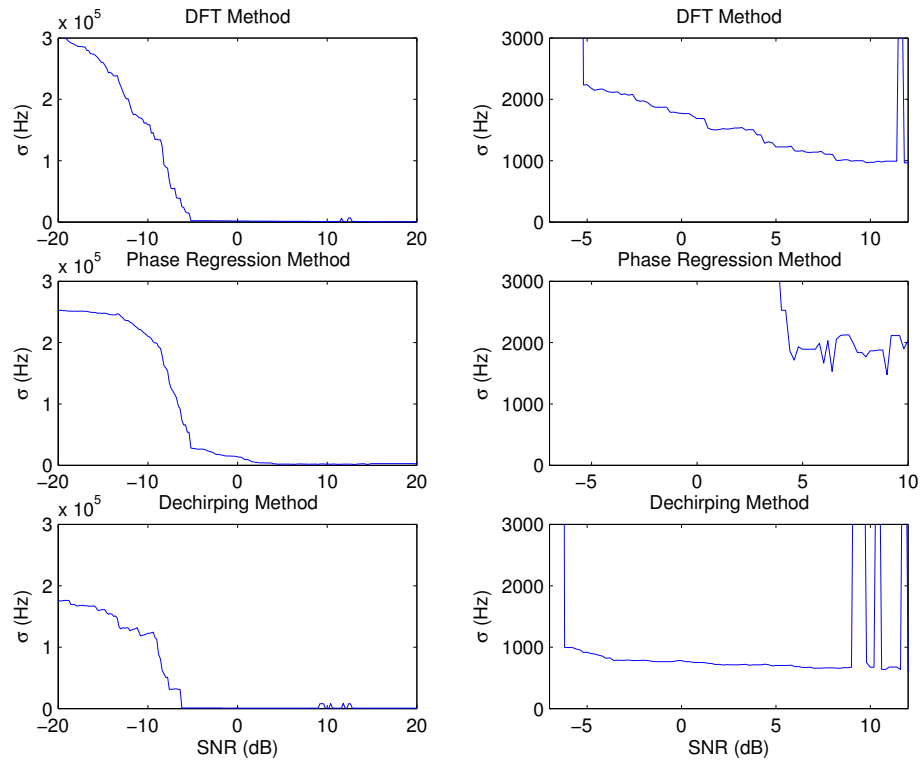


Figure 5.7: Standard deviation of center frequency estimates from the Doppler model as a function of SNR using the September 2002 data set. The three plots to the right are the same plots to the left with axes changed to examine the SNR intervals where the center frequency estimates converge to the Doppler model. The top plots reveal the performance of the Doppler model in fitting estimates obtained by the DFT method; the middle plots correspond the phase regression method; and the bottom plots are obtained using the dechirping method.

to converge until about 5 dB SNR with a standard deviation of approximately 2 kHz. The number of pulses considered in the model is halved at 5 dB SNR compared to the number considered at -5 dB. As a result, very few pulses are included in the Doppler model, leading to questionable outcomes. Use of the dechirping method leads to a Doppler model that converges above -6 dB with standard deviation below 1 kHz. This method yields the lowest variance. Estimates of Doppler compensation and Doppler shift yield the same trends (Fig. 5.8). The DFT and dechirping methods yield reasonable results when enough pulses are included, while the phase regression method cannot use enough pulses to accurately estimate Doppler parameters.

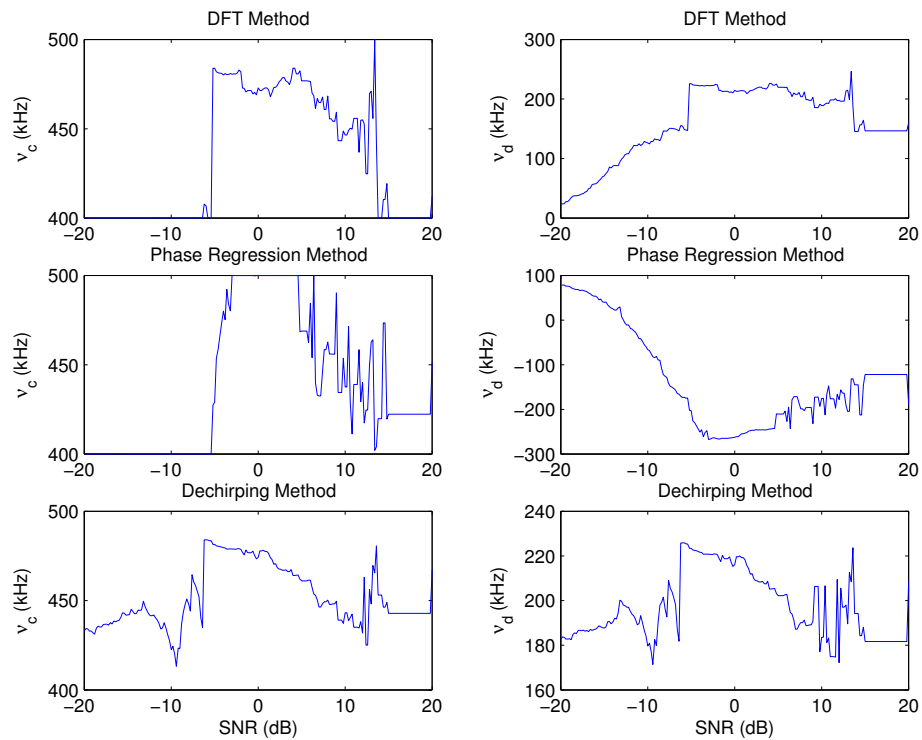


Figure 5.8: Doppler compensation and Doppler shift estimates as a function of SNR threshold using the September 2002 data set. The DFT method reveals a stable model estimate of Doppler compensation and Doppler shift between -5 and -2 dB SNR. However, the phase regression method does not reveal a consistent estimate at any SNR. The dechirping method converges for SNR between -6 and -2 dB.

Table 5.1: Comparison of SeaWinds Performance over Time using CGS Data Sets

Start Time (UTC)	Beam	Pulses	σ (kHz)	ν_c (kHz)	ν_d (kHz)
2002/09/30 12:34:22	Outer Approaching	149	0.82	479.63	221.63
2002/09/30 12:38:31	Outer Receding	151	0.87	480.11	-230.27
2002/09/30 12:34:45	Inner Approaching	119	4.45	437.41	194.70
2002/09/30 12:38:09	Inner Receding	138	1.02	434.07	-212.31
2003/01/24 01:29:28	Outer Approaching	144	0.75	483.43	211.17
2003/01/24 01:33:32	Outer Receding	161	0.80	484.19	-214.91
2003/01/24 01:30:09	Inner Approaching	184	0.74	431.25	166.82
2003/01/24 01:33:09	Inner Receding	129	2.33	428.86	-199.76
2004/07/08 01:19:22	Outer Approaching	134	0.70	483.84	154.91
2004/07/08 01:22:26	Outer Receding	158	0.69	484.42	-165.29
2004/07/08 01:20:17	Inner Approaching	163	1.61	432.63	71.53
2004/07/08 01:21:31	Inner Receding	169	0.72	431.53	-77.19

5.5 Evaluation of SeaWinds Performance over Time

Of the three estimation methods, the dechirping method is the most accurate. It is chosen to evaluate SeaWinds performance over a two-year span. Due to computational intensity and lack of resources at this time, data observation is limited to three data sets from September 2002, January 2003, and July 2004. These dates were chosen to provide sufficient coverage of the SeaWinds instrument over the last two years. A later date in 2003 is not available since the CGS was configured to receive data from SeaWinds on ADEOS-II during that year.

Table 5.1 shows the results of the Doppler model using the dechirping method on three data sets with an SNR threshold of -4 dB. These values were generated from the models shown in Figs. 5.9 to 5.14, which show the inner and outer beams approaching and receding from the CGS. The magnitude of the Doppler compensation sinusoid nominally approaches values of 480 kHz for the outer beam and 430 kHz for the inner beam. However, the Doppler shift values can vary widely due to the orbital geometry of the satellite with respect to the CGS. Doppler shifts are not expected to exceed a magnitude of 240 kHz for the outer beam and 215 kHz for the inner beam.

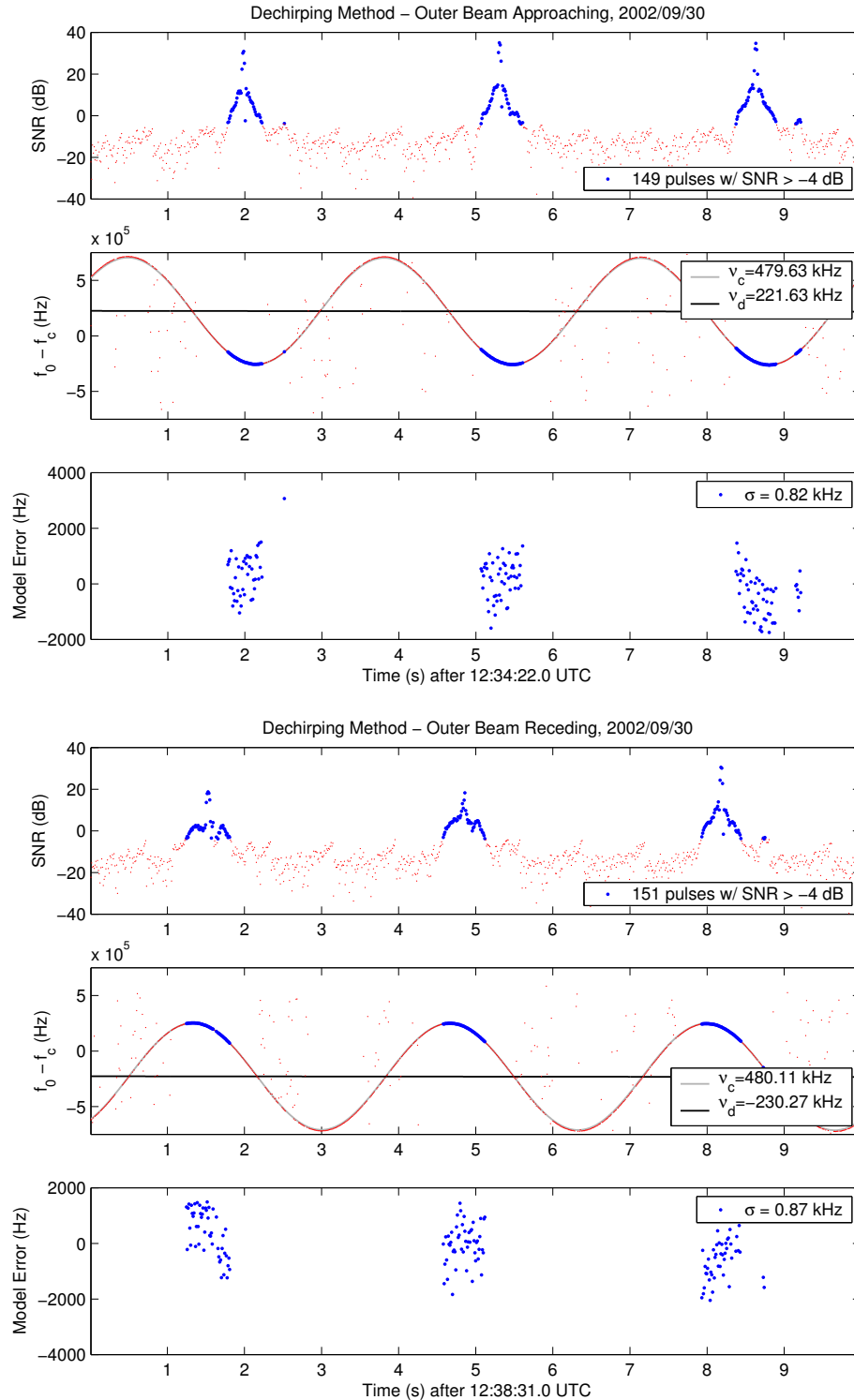


Figure 5.9: Outer beam approaching and receding from the CGS in September 2002. Doppler shift ν_d is positive when the beam approaches the CGS and negative when it recedes. As SeaWinds flies by, the CGS is generally illuminated at points of maximum Doppler compensation. In this capture, the amplitude of the Doppler compensation sinusoid is approximately $\nu_c = 480$ kHz, the nominal value for the outer beam. The difference between the magnitude of the Doppler shifts is only 8.64 kHz.

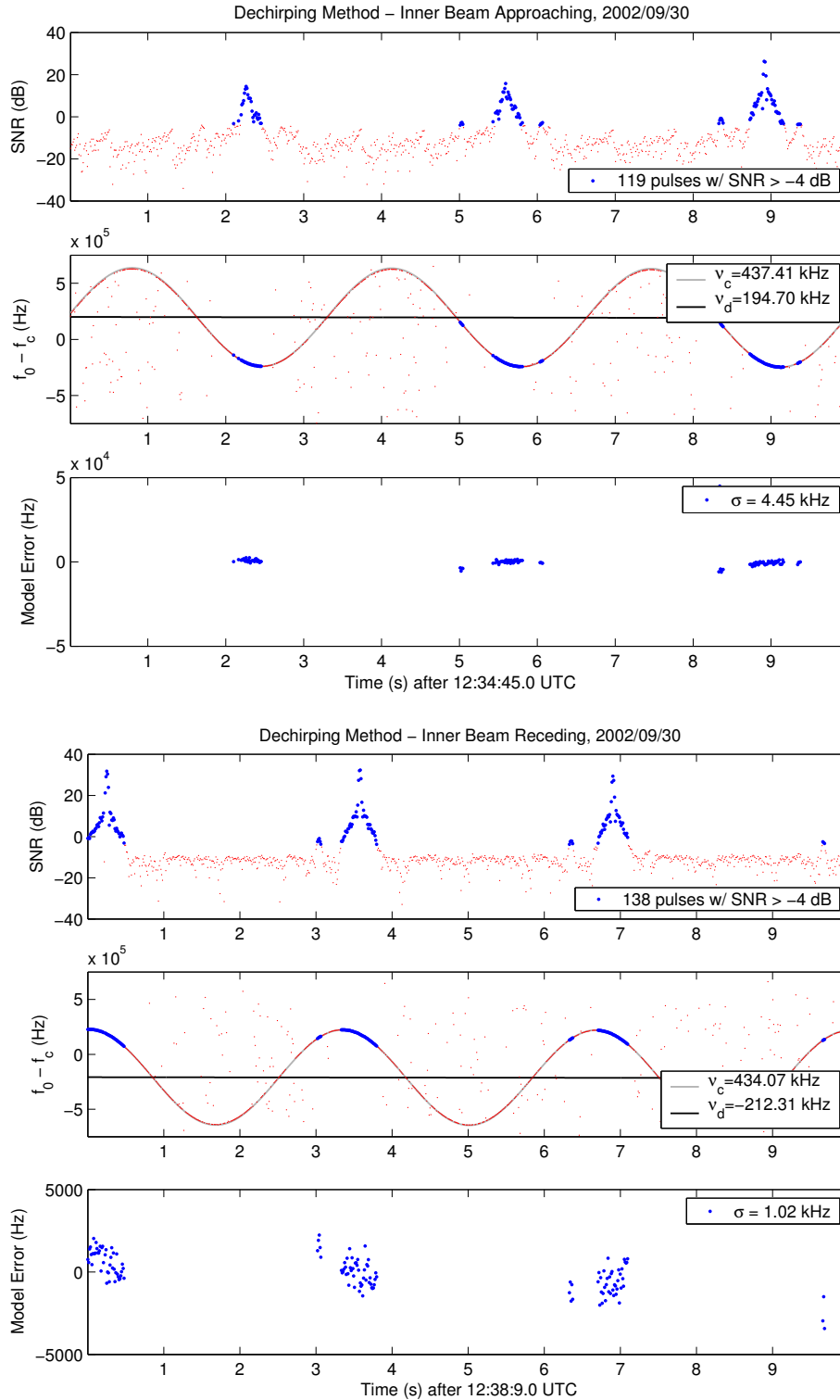


Figure 5.10: Inner beam approaching and receding from the CGS in September 2002. The amplitude of the Doppler compensation sinusoid is approximately $\nu_c = 436$ kHz, close to the nominal value of $\nu_c = 430$ kHz for the inner beam. The difference between the magnitude of the Doppler shifts is 17.61 kHz.

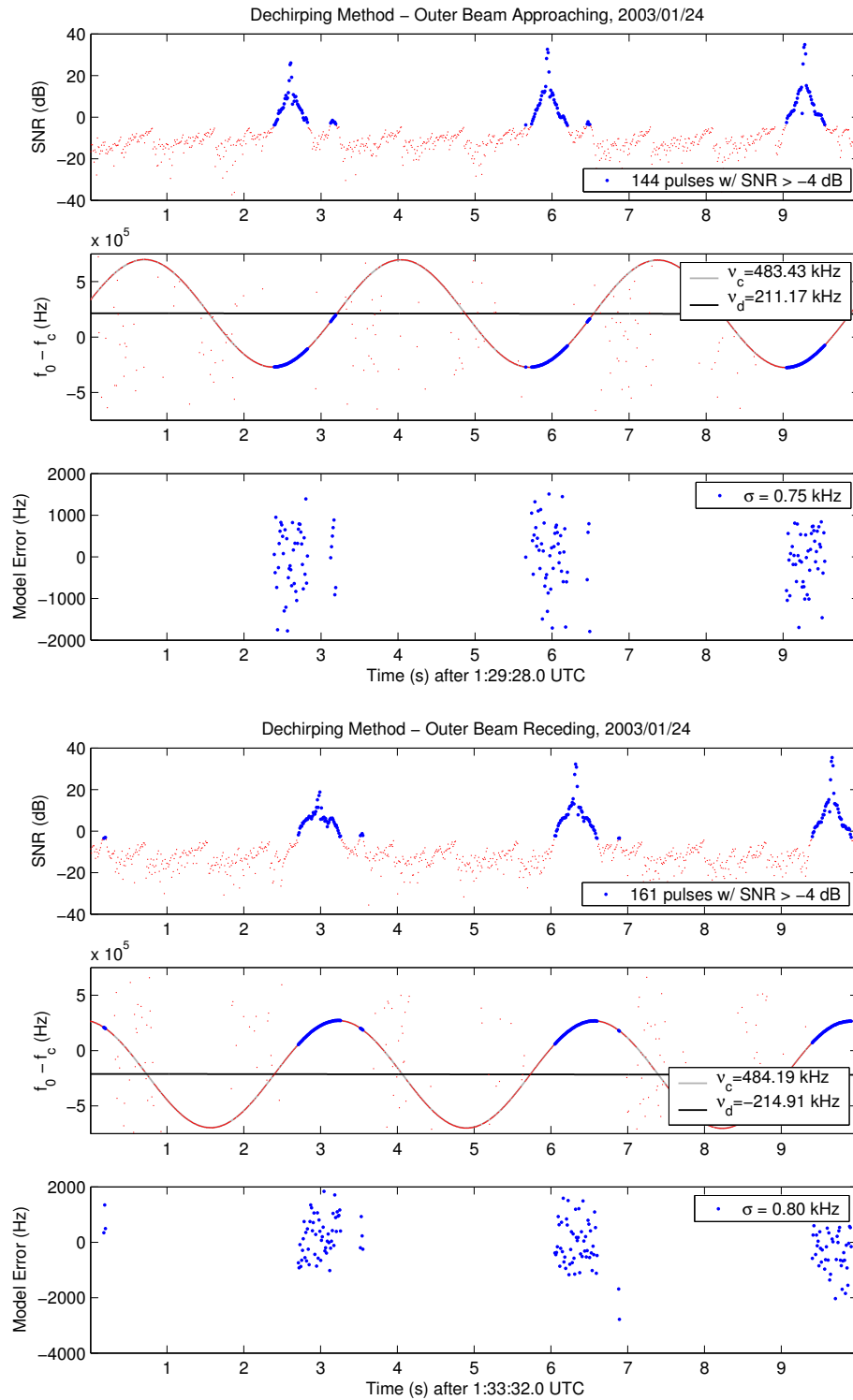


Figure 5.11: Outer beam approaching and receding from the CGS in January 2003. In this capture, the amplitude of the Doppler compensation sinusoid is approximately $\nu_c = 484$ kHz, near the nominal value for the outer beam. The difference between the magnitude of the Doppler shifts is only 3.74 kHz.

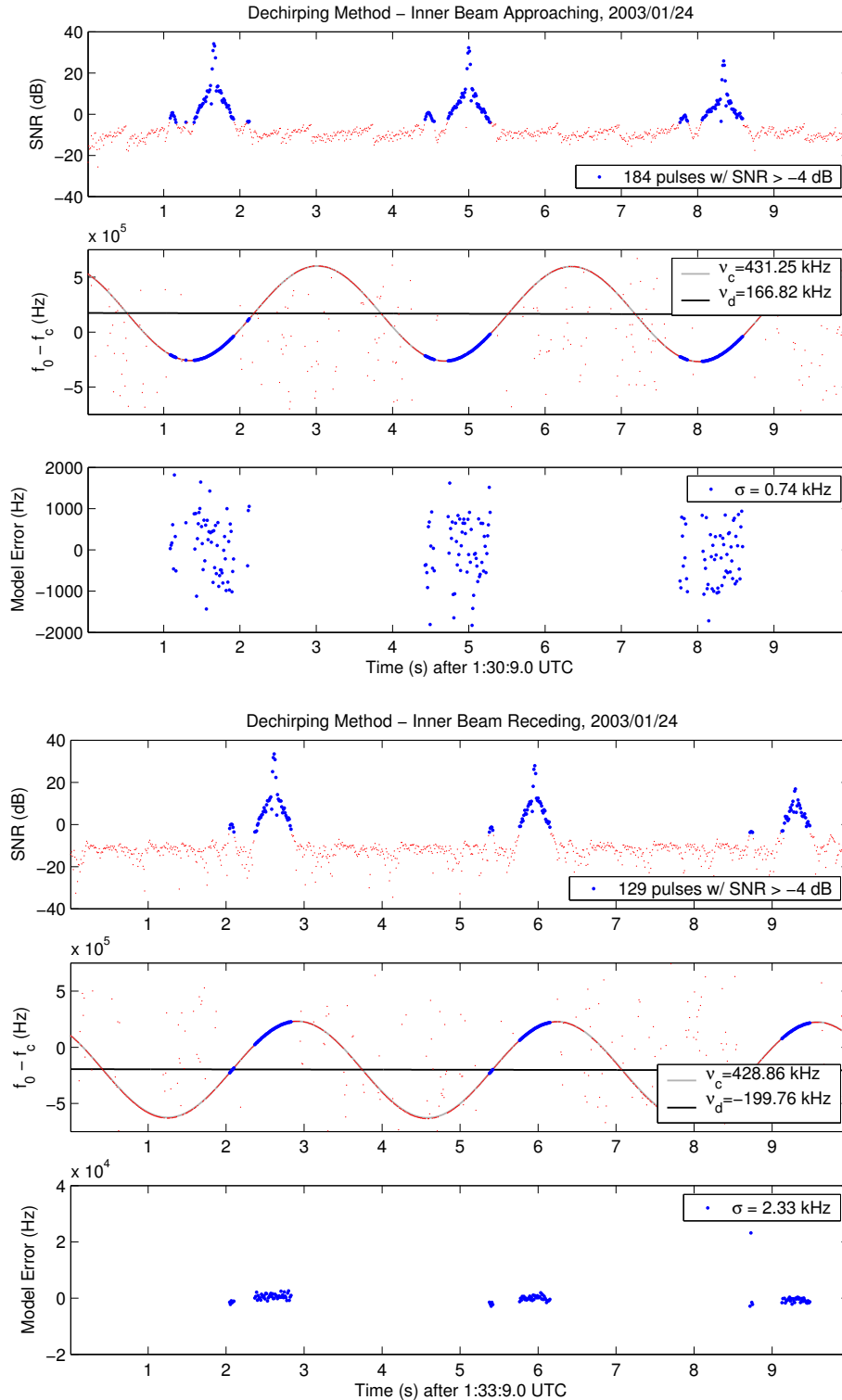


Figure 5.12: Inner beam approaching and receding from the CGS in January 2003. The amplitude of the Doppler compensation sinusoid is approximately $\nu_c = 430$ kHz, the nominal value for the inner beam. The difference between the magnitude of the Doppler shifts is 32.94 kHz.

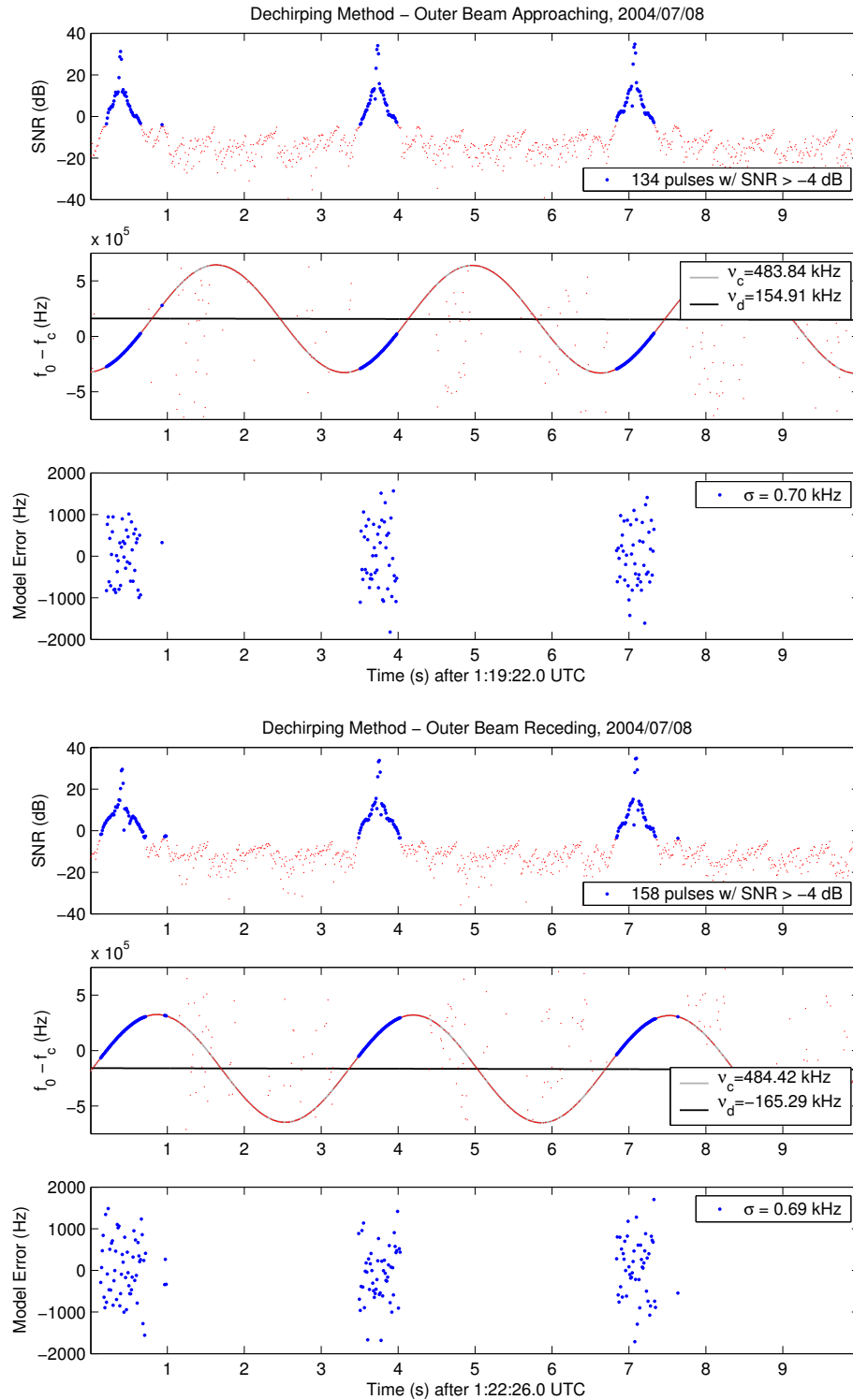


Figure 5.13: Outer beam approaching and receding from the CGS in July 2004. In this capture, the amplitude of the Doppler compensation sinusoid is approximately $\nu_c = 484$ kHz, near the nominal value for the outer beam. The difference between the magnitude of the Doppler shifts is only 10.38 kHz.

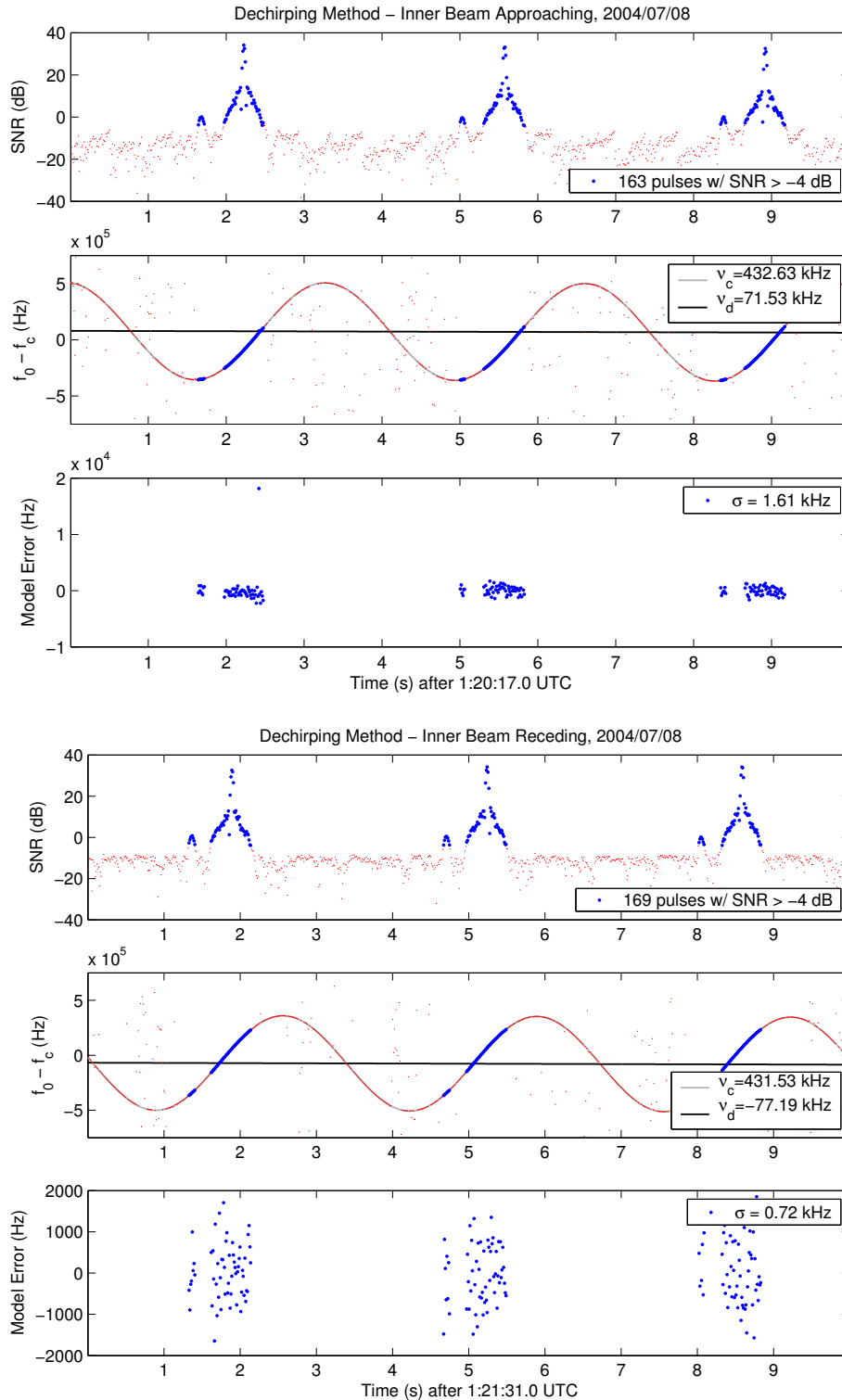


Figure 5.14: Inner beam approaching and receding from the CGS in July 2004. The amplitude of the Doppler compensation sinusoid is approximately $\nu_c = 432$ kHz, near the nominal value for the inner beam. The difference between the magnitude of the Doppler shifts is 5.66 kHz.

5.6 Summary

The DFT method performs modestly by yielding a Doppler model with standard deviation within 2 kHz of estimated center frequencies. The dechirping method improves this standard deviation to 1 kHz. Its performance is limited by accuracy of arrival time estimates, which is limited by sample rate to 48 Hz. A higher sample rate and better arrival time estimation methods can improve performance of the dechirping method.

The Doppler model reveals the Doppler compensation algorithm is performing correctly. Observation of carrier frequency drift is not determinable without telemetry data since a frequency bias can be mistaken for a Doppler shift. A blind method to observe drift assumes nominal center frequency and compares the magnitudes of the Doppler shifts as SeaWinds approaches and recedes from the CGS. By subjectively observing the Doppler shift from each beam, no drift of SeaWinds carrier frequency can be substantiated.

Chapter 6

Conclusion

The Calibration Ground Station is essential to verify correct operation of the SeaWinds scatterometer. This verification helps NASA JPL to improve the accuracy of their data products, thereby furthering the ability to understand the Earth's environment.

In this thesis, the operation of the SeaWinds instrument and the Calibration Ground Station are analyzed. Several issues are identified that complicate the estimation of SeaWinds signal parameters. A significant limitation is that the SeaWinds instrument illuminates the CGS in sweeps. As a result, only a small portion of the pulses received by the CGS emerge from the noise floor. The major obstacle to estimating pulse parameters is determining the arrival times of these pulses in low SNR.

A linear FM model is imposed on SeaWinds transmissions in order to allow parametric estimation of pulse parameters such as chirp rate and center frequency. The Doppler shift is factored into the signal phase, and expected ranges of parameters are found. A modified discrete analytic signal is introduced that eliminates the positive frequency spectrum, creating a complex signal of the appropriate spectrum. The concept of SNR defined over alternate signal spaces is explained, and several time-frequency transforms are shown to resolve linear FM waveforms. These transforms culminate in the Radon transform of the Wigner Distribution, which is a maximum likelihood estimator of linear FM waveform parameters.

Estimation of pulse arrival times via envelope detection is analyzed and three frequency estimation methods are compared. While the DFT and phase regression methods are computationally efficient, the dechirping matched filter bank method yields the best estimator performance at low SNR. The DFT method can be used for quickly obtaining

rough frequency estimates. The phase regression method is recommended only for pulses with SNR greater than 8 dB.

These frequency estimation methods are applied to real SeaWinds data captures. The Doppler compensation algorithm is verified to be working properly. This was not previously possible because only high-SNR portions of data were originally considered. Without telemetry data, drift of the SeaWinds carrier frequency cannot be observed since it cannot be easily distinguished from Doppler shift. However, a subjective observation of the Doppler shift in several SeaWinds passes does not substantiate carrier drift.

Future research is needed to develop an effective algorithm that estimates the arrival times of pulses that are buried in noise. This will increase the ability to accurately estimate parameters of the pulses. This thesis focuses on single pulse estimation. Future work on multiple pulse estimation using these techniques will enable improved estimation of the SeaWinds parameters. Finally, the effects of nonconstant signal amplitude on parameter estimation of linear FM pulses needs to be studied.

APPENDIX

Appendix A

CGS Maintenance and Installation

Meticulous hardware and software maintenance is required to sustain the CGS and archive its data for post processing. Over the course of the project, I completed the following tasks as part of my research:

1. Converted the CGS to receive SeaWinds transmissions from QuikSCAT after the power failure of the ADEOS-II satellite.
2. Maintained CGS hardware and software to correctly capture SeaWinds transmissions.
3. Archived captured data on a daily basis; backed up these archives to CD-R.

After installation of the CGS at BYU, the Provo location was studied to determine if the CGS yields accurate measurements and if the SeaWinds instrument illuminates the ground station on a relatively frequent basis. A simplified geometric analysis was used to determine the elevation angles of various peaks in the surrounding Utah County (Fig. A.1). Data extracted from the United States Geological Survey GNIS Database was used to compute the elevation angles of significant peaks relative to the CGS. From a GPS unit, the coordinates of the CGS are $40^{\circ} 14' 48.3''$ N, $111^{\circ} 38' 52.0''$ W, at an altitude of 1428 m. The largest elevation angle was found to belong to Y Mountain (to the east of the CGS) at $17^{\circ} 42'$. This indicates that Y Mountain does not physically impede the CGS from receiving a line-of-sight (LOS) transmission from the main lobes of the SeaWinds antenna beams.

To verify these results, on October 24, 2002, a student from the BYU Civil Engineering Department surveyed the area surrounding the CGS. The summit of Y Mountain

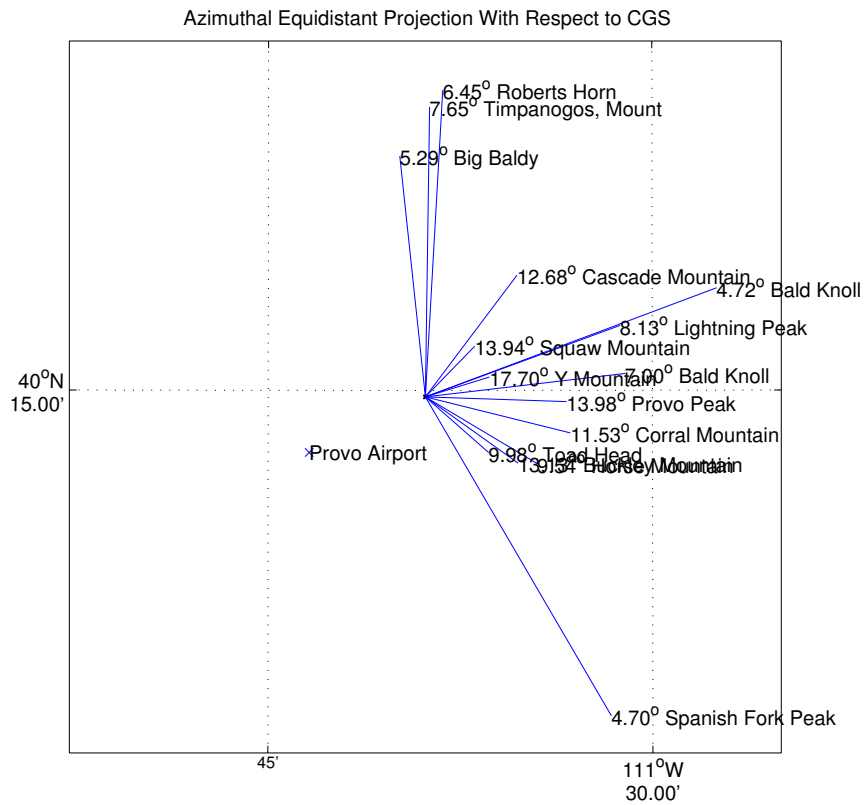


Figure A.1: Elevation angles of significant mountains in Utah County. Lines emanating from the CGS reveal its position with respect to each mountain.



Figure A.2: Nick Williams, a BYU Civil Engineering Student, surveys Y Mountain to measure the elevation angle of its summit.

presented the largest elevation angle and was surveyed at $19^{\circ} 28' 5'' \approx 19.5^{\circ}$. The difference between the calculated and measured elevation angle may be explained by protrusions that block the summit of Y Mountain from being observed by the CGS, even though the summit is higher in elevation.

Bibliography

- [1] P. K. Yoho, "Satellite scatterometers: Calibration using a ground station and statistical measurement theory," Ph.D. dissertation, Brigham Young University, Provo, UT, Dec. 2003. [Online]. Available: <http://contentdm.lib.byu.edu/ETD/image/etd306.pdf>
- [2] A. Anderson, "Analysis and usage of the Quikscat Calibration Ground Station," Master's thesis, Brigham Young University, Provo, UT, Aug. 2001.
- [3] J. T. Adams, "Ground calibration of an orbiting spacecraft radar transmitter," Master's thesis, University of California at Los Angeles, Los Angeles, CA, 1999. [Online]. Available: http://www.jonadams.com/pages/thesis/Ground_Calibration_of_an_Orbiting_Spacecraft_Radar_Transmitter.htm
- [4] C. Wu, Y. Liu, K. H. Kellogg, K. S. Pak, and R. L. Glenister, "Design and calibration of the Seawinds scatterometer," vol. 39, pp. 94–109, Jan. 2003.
- [5] R. D. Crowley, "Hardware design overview of a satellite scatterometer," in *Southeastcon '98*, Apr. 1998, pp. 244–247.
- [6] J. A. Johnston, "Wigner distribution and FM radar signal design," in *Radar and Signal Processing, IEE Proceedings F*, vol. 136, Apr. 1989, pp. 81–88.
- [7] D. K. Barton, C. E. Cook, and P. Hamilton, Eds., *Radar Evaluation Handbook*. Boston: Artech House, 1991.
- [8] V. C. Chen, *Time-Frequency Transforms for Radar Imaging and Signal Analysis*. Boston: Artech House, 2002.
- [9] X.-G. Xia, "A quantitative analysis of SNR in the short-time fourier transform domain for multicomponent signals," vol. 46, pp. 200–203, Jan. 1998.

- [10] B. R. Mahafza, *Radar Systems Analysis and Design Using MATLAB*. New York: Chapman & Hall/CRC, 2000.
- [11] C. E. Cook and M. Bernfeld, *Radar Signals: An Introduction to Theory and Application*. New York: Academic Press, 1967.
- [12] L. Cohen, *Time-Frequency Analysis*. Englewood Cliffs, NJ: Prentice Hall PTR, 1995.
- [13] S. L. Marple, Jr., “Computing the discrete-time ‘analytic’ signal via FFT,” vol. 47, pp. 2600–2603, Sept. 1999.
- [14] M. H. Hayes, *Statistical Digital Signal Processing and Modeling*. New York: Wiley, 1996.
- [15] A. V. Oppenheim, R. W. Schaffer, and J. R. Buck, *Discrete-Time Signal Processing*, 2nd ed. Upper Saddle River, NJ: Prentice Hall, 1998.
- [16] B. Boashash, “Heuristic formulation of time-frequency distributions,” in *Time Frequency Signal Analysis and Processing: A Comprehensive Reference*, B. Boashash, Ed. Boston: Elsevier, 2003.
- [17] F. Hlawatsch, *Time-Frequency Analysis and Synthesis of Linear Signal Spaces: Time-Frequency Filters, Signal Detection and Estimation, and Range-Doppler Estimation*. Boston: Kluwer Academic Publishers, 1998.
- [18] S. Kay and G. F. Boudreaux-Bartels, “On the optimality of the wigner distribution for detection,” in *IEEE International Conference on Acoustics, Speech, and Signal Processing 1985*, vol. 10, Apr. 1985, pp. 1017–1020.
- [19] J. C. Wood and D. T. Barry, “Radon transformation of time-frequency distributions for analysis of multicomponent signals,” vol. 42, pp. 3166–3177, Nov. 1994.
- [20] A. K. Jain, *Fundamentals of Digital Image Processing*. Upper Saddle River, NJ: Prentice Hall, 1989.
- [21] W. Li, “Wigner distribution method equivalent to dechirp method for detecting a chirp signal,” vol. 35, pp. 1210–1211, Aug. 1987.

- [22] J. T. Adams and J. P. Lux, "Ground calibration of an orbiting spacecraft transmitter," in *Aerospace Conference Proceedings, 2000 IEEE*, vol. 5, Mar. 2000, pp. 37–49.
- [23] S. M. Kay, *Fundamentals of Statistical Signal Processing: Detection Theory*. Upper Saddle River, NJ: Prentice Hall PTR, 1998.
- [24] G. F. Boudreaux-Bartels, "Mixed time-frequency signal transformations," in *The Transforms and Applications Handbook*, A. D. Poularikas, Ed. Boca Raton, FL: CRC Press, 1995, ch. 12.
- [25] P. Flandrin, "Ambiguity functions," in *Time Frequency Signal Analysis and Processing: A Comprehensive Reference*, B. Boashash, Ed. Boston: Elsevier, 2003.
- [26] D. C. Ghiglia and M. D. Pritt, *Two-Dimensional Phase Unwrapping: Theory, Algorithms, and Software*. New York: Wiley, 1998.
- [27] P. M. Djurić and S. M. Kay, "Parameter estimation of chirp signals," vol. 38, pp. 2118–2126, Dec. 1990.
- [28] S. A. Tretter, "Estimating the frequency of a noisy sinusoid by linear regression," vol. 31, pp. 832–835, Nov. 1985.
- [29] B. Boashash, "Estimating and interpreting the instantaneous frequency of a signal—part 2: Algorithms and applications," in *Proceedings of the IEEE*, vol. 80, Apr. 1992, pp. 540–568.
- [30] S. M. Kay, *Fundamentals of Statistical Signal Processing: Estimation Theory*. Upper Saddle River, NJ: Prentice Hall PTR, 1993.
- [31] I. Ali, N. Al-Dhahir, and J. E. Hershey, "Doppler characterization for LEO satellites," vol. 46, pp. 309–313, Mar. 1998.